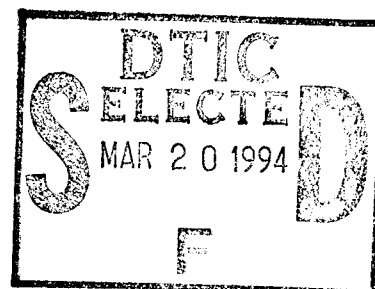


PL-TR-94-2234

ARCING PREDICTIONS FOR PASP PLUS SOLAR ARRAYS

**James D. Soldi, Jr.
Daniel E. Hastings**



**Massachusetts Institute of Technology
Space Power and Propulsion Laboratory
77 Massachusetts Avenue
Cambridge, MA 02139**

2 August 1994

Scientific Report No. 2

Approved For Public Release; Distribution Unlimited

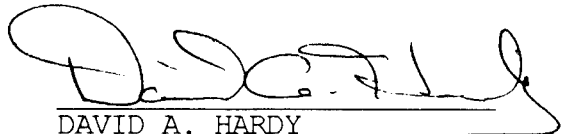


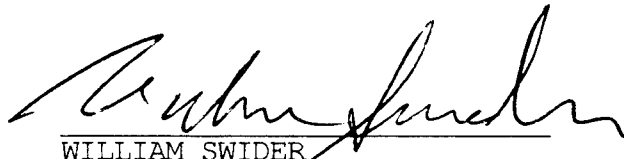
**PHILLIPS LABORATORY
Directorate of Geophysics
AIR FORCE MATERIEL COMMAND
HANSCom AIR FORCE BASE, MA 01731-3010**

19950317 130

This technical report has been reviewed and is approved for publication.


PAUL S. SEVERANCE
Contract Manager


DAVID A. HARDY
Branch Chief


WILLIAM SWIDER
Deputy Division Director

This report has been reviewed by the ESC Public Affairs Office (PA) and is releasable to the National Technical Information Service (NTIS).

Qualified requestors may obtain additional copies from the Defense Technical Information Center (DTIC). All others should apply to the National Technical Information Service (NTIS).

If your address has changed, or if you wish to be removed from the mailing list, or if the addressee is no longer employed by your organization, please notify PL/IM, 29 Randolph Road, Hanscom AFB, MA 01731-3010. This will assist us in maintaining a current mailing list.

Do not return copies of this report unless contractual obligations or notices on a specific document requires that it be returned.

REPORT DOCUMENTATION PAGE			Form Approved OMB No. 0704-0188	
Public reporting burden for this collection of information is estimated to average 1 hour per response, including the time for reviewing instructions, searching existing data sources, gathering and maintaining the data needed, and completing and reviewing the collection of information. Send comments regarding this burden estimate or any other aspect of this collection of information, including suggestions for reducing this burden, to Washington Headquarters Services, Directorate for Information Operations and Reports, 1215 Jefferson Davis Highway, Suite 1204, Arlington, VA 22202-4302, and to the Office of Management and Budget, Paperwork Reduction Project (0704-0188), Washington, DC 20503.				
1. AGENCY USE ONLY (Leave blank)		2. REPORT DATE 2 August 1994		3. REPORT TYPE AND DATES COVERED Scientific #2
4. TITLE AND SUBTITLE Arcing Predictions for PASP PLUS Solar Arrays			5. FUNDING NUMBERS PE 63410F PR 2822 TA 01 WU PP	
6. AUTHOR(S) James D. Soldi, Jr Daniel E. Hastings			Contract F19628-92-K-0016	
7. PERFORMING ORGANIZATION NAME(S) AND ADDRESS(ES) Massachusetts Institute of Technology Space Power and Propulsion Laboratory 77 Massachusetts Avenue Cambridge, MA 02139			8. PERFORMING ORGANIZATION REPORT NUMBER	
9. SPONSORING/MONITORING AGENCY NAME(S) AND ADDRESS(ES) Phillips Laboratory 29 Randolph Road Hanscom AFB, MA 01731-3010 Contract Manager: Capt Paul Severance/GPSP			10. SPONSORING/MONITORING AGENCY REPORT NUMBER PL-TR-94-2234	
11. SUPPLEMENTARY NOTES				
12a. DISTRIBUTION / AVAILABILITY STATEMENT Approved for public release; distribution unlimited			12b. DISTRIBUTION CODE	
13. ABSTRACT (Maximum 200 words) Future solar arrays are being designed for much higher voltages in order to meet high power demands at low currents. Unfortunately, negatively biased high voltage solar arrays have been observed to arc when exposed to the low earth orbit plasma environment. In previous work, analytical and numerical models of this arcing phenomenon on conventional solar cells have been developed which show excellent agreement with experimental data. The analytical model has been further developed to be more physically accurate and to be able to realistically model space experiments which will be operating in a widely changing environment. With this model, predictions were made for the solar array arcing on the upcoming Air Force Photovoltaic Array Space Power Plus Diagnostics (PASP Plus) experiment. These simulations predict arcing rates ranging from 0 to 4.3 arcs/second, depending on the array and the experimental and environmental conditions. It was found that the cell thickness plays a dominant role in relative arc rates between the various cells. The large simulated database generated was used to develop software that will be used to examine and analyze the flight data, extracting correlations between arc rate and the various material properties, environmental variables, and operational parameters.				
14. SUBJECT TERMS Solar array arcing High voltage solar arrays Space environmental interactions			15. NUMBER OF PAGES 50	
			16. PRICE CODE	
17. SECURITY CLASSIFICATION OF REPORT Unclassified	18. SECURITY CLASSIFICATION OF THIS PAGE Unclassified	19. SECURITY CLASSIFICATION OF ABSTRACT Unclassified	20. LIMITATION OF ABSTRACT SAR	

Contents

1	Introduction	1
1.1	Background	2
1.2	Overview of This Research	5
2	Semi-Analytic Model	8
2.1	EFEE Charging Time	9
2.2	Ion Charging Time	12
2.3	Arc Rate Code	12
3	Modifications to Semi-Analytic Arc Rate Code	16
4	PASP Plus Predictions	24
4.1	PASP Plus	24
4.2	Hardware Description	25
4.2.1	Diagnostic Equipment Description	25
4.2.2	Solar Array Module Descriptions	26
4.3	Experiment Simulation	28
4.3.1	Arcing Ranges	30
4.3.2	Orbital Simulation	31
5	Conclusions	37

Accession For	
NTIS	<input checked="" type="checkbox"/>
CRA&I	<input type="checkbox"/>
DTIC	<input type="checkbox"/>
TAB	<input type="checkbox"/>
Unannounced	<input type="checkbox"/>
Justification	
By	
Distribution /	
Availability Code	
Dist	Availability for Special
A-1	

List of Figures

1	Schematic of a Conventional Solar Cell	2
2	Model of the Conventional Solar Array Used for Numerical Simulations . .	4
3	Arcing Sequence of a High Voltage Solar Array	6
4	Geometry for EFEE charging	9
5	Typical Electric Field Run-Away	11
6	Flow Chart of Semi-Analytic Arc Rate Code	13
7	Minimum Charging Time	15
8	Flow Chart of Modified Arc Rate Code	17
9	Critical Ambient Neutral Density Variation with Temperature	21
10	Critical Ambient Neutral Density Variation with Temperature and Voltage .	22
11	Deployed APEX Spacecraft with PASP Plus Experiment	26
12	Range of Arc Rates for PASP Plus Conventional Cells	32
13	Range of Arcing Probability for PASP Plus Conventional Cells	33
14	Voltage Power Law Fit to Array #2 Arc Rate	34
15	Voltage Exponential Fit to Array #2 Arc Rate	35

List of Tables

1	PASP Plus Cell Data	28
2	PASP Plus Bias Voltages	29
3	PASP Plus Phase 1 Biasing Sequencing	30
4	Environmental Parameters for Minimum/Maximum Arcing	30
5	PASP Plus Conventional Cell Onset Voltages	31

List of Symbols

A	Fowler Nordheim coefficient ($1.54 \times 10^{-6} \times 10^{4.52\phi_W^{-1/2}} / \phi_W$ A/V ²)
B	Fowler Nordheim coefficient ($6.53 \times 10^9 \phi_W^{1.5}$ V/m)
C_{diele}	capacitance of dielectric (F/m ²)
C_{front}	capacitance of coverglass front surface (F)
d	thickness of dielectric (m)
d_1	thickness of coverglass (m)
d_2	thickness of adhesive (m)
d_{gap}	gap distance between cathode and anode (m)
d_i	distance of electron first impact point from triple junction (m)
d_o	overhang distance of coverglass (m)
d_o^c	critical overhang distance of coverglass (m)
E_e	electric field at emission site (V/m)
E_i	electron incident energy on dielectric plate (eV)
E_{max}	electron incident energy for maximum secondary electron yield (eV)
E_{TJ}	electric field at triple junction (V/m)
E_1	electric field of coverglass (V/m)
E_2	electric field of adhesive (V/m)
j_{ec}	electron current density from conductor (A/m ²)
j_{ee}	secondary electron current density from dielectric (A/m ²)
j_{FN}	Fowler-Nordheim current density from the conductor (A/m ²)
j_{id}	ion ram current density to the dielectric (A/m ²)
n_e	plasma number density (m ⁻³)
n_{es}	emission site number density (m ⁻²)
m_e	electron mass (kg)
m_i	ion mass (kg)
\dot{R}	arc rate (sec ⁻¹)
r_s	sheath radius (m)
S_{FN}	emission site area determined from F-N plot (m ²)

S_{real}	emission site area determined by accounting for electron space charge effects (m^2)
T_e	electron temperature (eV)
T_i	ion temperature (eV)
V_{arc}	voltage at which last arc occurred V
V_{bias}	bias voltage of interconnector/conductor V
V_e	voltage which minimizes arcing time V
V_i	initial voltage before solar cell charging V
v_{ion}	mean speed of ions entering sheath (m/sec)
v_x	electron velocity in the x direction (m/sec)
v_y	electron velocity in the y direction (m/sec)
y	distance of emission site from the triple junction (m)
β	field enhancement factor
ΔQ	charge lost from one coverglass by one discharge (C)
ϵ_{d_1}	relative dielectric constant of coverglass
ϵ_{d_2}	relative dielectric constant of adhesive
\mathcal{E}_1	energy at $\gamma_{ee} = 1$ (eV)
ϕ_c	potential of conductor (V)
ϕ_i	potential of coverglass-adhesive interface (V)
ϕ_w	work function (eV)
γ_{ee}	secondary electron yield
γ_{max}	maximum secondary electron yield at normal incidence
η	factor accounting for difference in electric field at emission site and triple junction
θ_i	incident impact angle of electron onto the dielectric surface
σ	surface charge density (C/m^2)
τ_{arc}	time between arcs (sec)
τ_{efee}	EFEE charging time (sec)
τ_{ion}	ion charging time (sec)
τ_{exp}	experiment time (sec)
ξ	factor accounting for difference of dielectric constants between coverglass and adhesive

Chapter 1

Introduction

Photovoltaic power systems continue to be the most commonly used means of meeting power needs for both DoD and commercial satellites. Currently, most systems operate at low voltage levels, typically 28 volts. Future space missions, however, will have higher power requirements than current systems, with power levels of 10kW to 1MW needed. To meet these requirements, either high current or high voltage systems can be used. The use of high current is undesirable for two reasons. First, high current systems require more massive power distribution cables, increasing the mass of the spacecraft. And second, high current results in higher resistive losses during the power transmission. Thus, high voltage power generation and transmission at low currents is desirable. For example, the Space Station Freedom design calls for power to be provided by high-voltage solar cells operating at 160V. Here, the term high voltage means that the absolute value of the bias voltage is on the order of 100V to 1000V.

A schematic of a conventional geometry solar cell is shown in Figure 1. The solar cell semi-conductor is protected by a coverglass glued to the top surface. This coverglass is used primarily to protect the cell from the radiation environment. The semiconductor itself is composed of two parts: an n-type semiconductor and a p-type semiconductor. A current path is set up between the cells by the use of metal interconnectors from the n-type semiconductor on one cell to the p-type semiconductors of the neighboring cells. Series of solar cells are used to achieve the desired voltage levels and parallel connected cells give the desired current levels.

When high-voltage solar arrays are placed in orbit, they interact with the ambient plasma environment. The steady state current collected by the solar arrays from the plasma must obey the zero net current condition, given by,

$$\frac{\partial \rho}{\partial t} + \nabla \cdot \vec{j} = 0, \quad (1)$$

which is derived from Gauss' and Ampere's Law. This causes part of the array to float

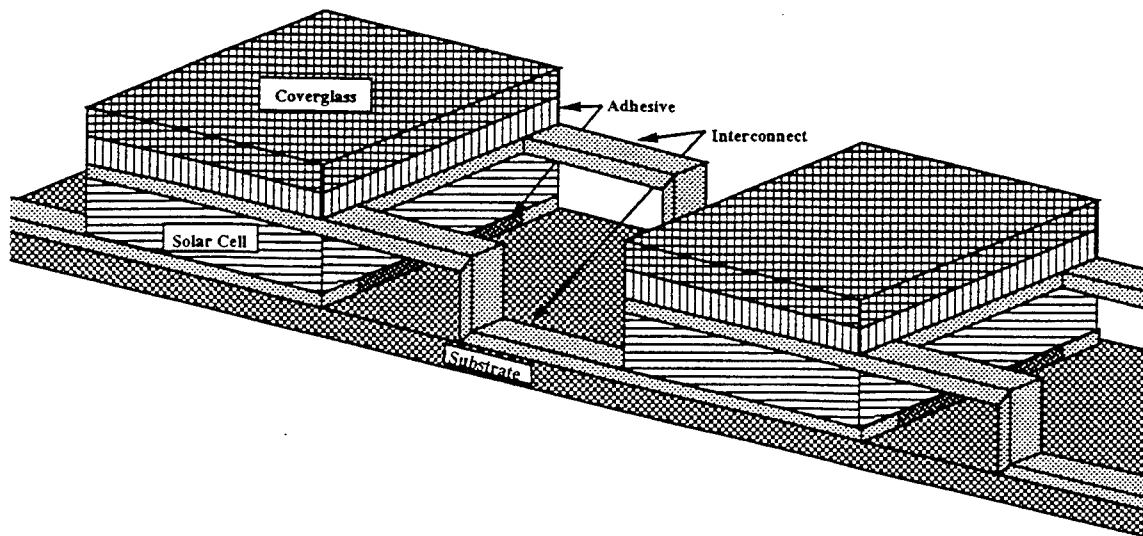


Figure 1: Schematic of a Conventional Solar Cell

positive with respect to the plasma, and thus collect electrons, and the rest to float negative and collect ions. Because electrons have a much higher mobility than the ions, the electron flux is higher than the ion flux, causing most of the array to float negative with respect to the plasma.

High-voltage solar arrays have been found to interact with the ambient space plasma environment in several manners, including current leakage³², arc discharges¹³, and enhanced drag due to Coulomb collisions¹⁰. For positive voltage operation, the current collection can become anomalously large, a phenomenon known as “snapover”. This can result in a significant leakage power loss. For large negative voltage operation, arc discharges have been found to occur. Arcing is typically defined as a sudden current pulse up to the order of an ampere on a timescale of a microsecond or less. The current pulse is often accompanied by a spot of light at the edge of the coverglass. Arcing can result in electromagnetic interference and solar cell damage.

1.1 Background

Arcing on high voltage solar arrays has been observed in both ground and space experiments. It was first observed by Herron et al.¹³ during plasma chamber tests of solar arrays biased between $\pm 16\text{kV}$. During the tests, arcing was found to occur at bias voltages as low as -6kV with a plasma density of 10^8m^{-3} . The first Plasma Interactive Experiment (PIX)⁷, launched in 1978 as an auxiliary payload on Landsat 3’s Delta rocket, verified the occurrence of arc discharges in the space environment. The experiment resulted in four hours of data taken in a polar orbit at 920km, during which time a solar array consisting of twenty-four conventional $2\text{cm} \times 2\text{cm}$ silicon solar cells were biased between ± 1000 volts. The cells were found to arc

at voltages greater than -750 volts.

A more extensive space experiment was conducted in 1983 aboard PIX II⁸, which was again launched as an auxiliary payload aboard a Delta launch vehicle into a 900km polar orbit. Approximately 18 hours of data were taken for an array consisting of 500 cells similar to those used in PIX I. During this experiment, arcing was found to occur for voltages as low as -255 volts.

Interpretation of the PIX II data was hampered by unexpected tumbling of the spacecraft, resulting in the Langmuir probe being placed in the wake during portions of the experiment, as well as power supply shutdowns following arcs. The data from the PIX II flight and ground tests were studied by Ferguson⁵, who assumed that the arc rate was linearly proportional to the plasma density and found that the arc rate then followed a power law dependence on the bias voltage, given by

$$R = 1.4 \times 10^{-10} (-V)^{3.093} \left(\frac{n}{6.3 \times 10^3} \right) \quad (2)$$

for the flight data, and

$$R = 1.82 \times 10^{-18} (-V)^{5.51} \quad (3)$$

for the ground tests at high density, where V is the bias voltage and n is the plasma density in cubic centimeters.

There have been two types of theoretical models proposed for the arcing onset mechanism. The first, proposed by Parks et al.²⁵, attributes the arcing onset to the Malter effect at a thin dielectric layer on the conductor surface. The second model, by Cho and Hastings³ based on previous work by Hastings et al.¹², attribute the arc to a gas discharge in neutral gases desorbed from the dielectric surface.

The model by Parks et al.²⁵ consists of the following scenario:

- (1) A dielectric impurity layer is formed on the conductor surface.
- (2) Ions attracted to the negative bias of the conductor are accumulated on the dielectric layer and enhance the electric field in the layer.
- (3) Fowler-Nordheim field emission causes electrons to be emitted from the conductor into the dielectric.
- (4) The electrons emitted from the metal surface have ionization collisions while being accelerated within the dielectric, leaving positive charges behind as they are emitted from the dielectric-vacuum interface.
- (5) This remaining positive charge further enhances the electric field within the dielectric layer.
- (6) The resulting rate of change of the electric field in the insulating layer is given by

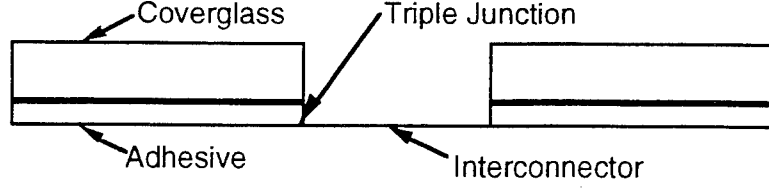


Figure 2: Model of the Conventional Solar Array Used for Numerical Simulations

$$\epsilon \frac{d}{dt} (\epsilon_r E_{m-d} - E_{d-v}) = j_i + j_{m-d} e^{\alpha_d d_d} P_{d-v} - j_{m-d}, \quad (4)$$

where ϵ_r is the dielectric constant of the insulating layer, E_{m-d} is the electric field in the dielectric layer, E_{d-v} is the ambient electric field at the dielectric-vacuum interface, j_i is the ion current density, α_d is the ionization rate per unit distance inside the layer, d_d is the dielectric layer thickness, P_{d-v} is the probability that the electrons are emitted from the dielectric-vacuum interface, and j_{m-d} is the Fowler-Nordheim emission current at the metal-dielectric interface given by

$$j_{m-d} = A E_{ins}^2 e^{-\frac{B}{E_{m-d}}}, \quad (5)$$

where A and B are the Fowler-Nordheim emission coefficients given by

$$A = \frac{1.54 \times 10^{-6} 10^{4.52/\sqrt{\phi_w}}}{\phi_w}, \quad (6)$$

$$B = 6.53 \times 10^9 \phi_w^{1.5}, \quad (7)$$

where ϕ_w is the work function of the metal in eV.

If the factor $e^{\alpha_d d_d} P_{d-v}$ is greater than unity, a positive feedback mechanism is created at the metal-dielectric interface, leading to a runaway of the field and the emission current by increasing E_{m-d} monotonically in time.

A second arcing onset mechanism was proposed by Cho and Hastings³, who studied the model system shown in Figure 2. This system was used to study the arc initiation process at the triple junction of the plasma, dielectric, and conductor.

The resulting arcing onset mechanism, used in this research, can be summarized by the following sequence, illustrated in Figure 3:

- (1) Ambient ions charge the dielectric (i.e. coverglass and adhesive) front surface, but leave the dielectric side surface uncharged.
- (2) As the front surface potential approaches zero relative to the plasma, a strong electric field of $E=V/d$ (where V is the bias voltage and d is the dielectric thickness) is formed at the conductor surface, inducing pre-breakdown electron emission due to enhanced field

electron emission (EFEE). Electrons are also released due to ion induced emission from ion bombardment of the conductor surface.

(3) Some of the emitted electrons strike the dielectric side surface, inducing the release of secondary electrons and causing electron stimulated desorption of neutrals adsorbed on the dielectric surface. If the secondary electron yield is greater than unity the side surface charges up positively, providing a positive feedback mechanism to further enhance the electric field at the conductor surface.

(4) As the electric field increases, the electron emission current increases until it is limited by the negative space charge of the emitted electrons.

(5) Once the neutral density becomes high enough, ionization begins due to collisions between electrons and neutrals.

(6) If the neutral density is very high, Townsend breakdown occurs. Even if the density is not high enough for Townsend breakdown to occur, breakdown is still possible if the positive ion space charge can cancel the negative electron space charge and enhance the field at the conductor.

(7) The arcing time is the minimum of the sum of the ion and EFEE charging times for all the emission sites on the conductor.

(8) A discharge wave created by the arc resets the charging process at all of the emission sites within the area covered by the wave.

This model was produced through the use of computer particle simulations of the arc initiation process. These results were then used to develop analytical formulas for the ion charging time τ_{ion} and the enhanced field electron emission charging time τ_{efee} . From this, a semi-analytic computer code was developed to predict the arc rates for high voltage solar arrays placed in a plasma environment. Subsequent work by Mong and Hastings²² used variations of the particle simulation and semi-analytic codes to explore the arcing characteristics of wrap-through-contact cells and to examine various arc mitigation techniques.

1.2 Overview of This Research

The focus of this research was twofold: to modify the semi-analytic simulation to be more physically accurate, and then to use this tool to predict the arc rates for the upcoming Air Force Photovoltaic Array Space Power Plus Diagnostics (PASP Plus) experiment. Predictions were made using expected environmental and operational parameters for the experiment. The data from the experiment will then be used, along with the simulations, to determine correlations between arc rate and the various material properties, environmental

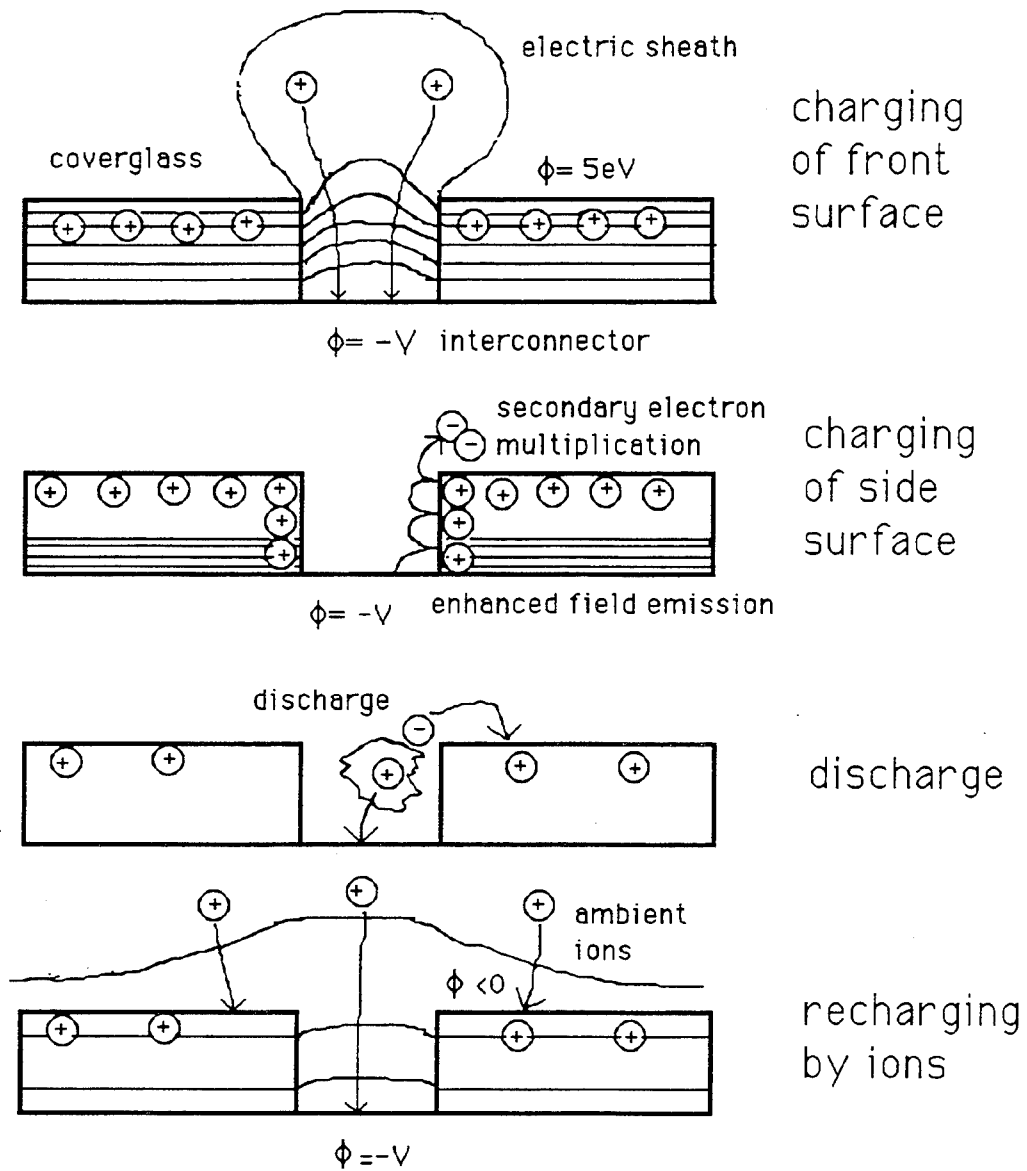


Figure 3: Arcing Sequence of a High Voltage Solar Array

variables, and experimental parameters.

In Chapter 2 the semi-analytic simulation developed by Cho and Hastings will be outlined, while Chapter 3 will discuss the modifications made to the code to make it more physically and experimentally accurate. The arc rate predictions for PASP Plus made using the code will then be discussed in Chapter 4. Finally, conclusions will be summarized in Chapter 5.

Chapter 2

Semi-Analytic Model

Figure 3 schematically shows the arcing sequence assumed in this research. This chapter will review the semi-analytic model of this sequence developed by Cho and Hastings, and the next chapter will discuss the modifications made to the model.

When an arc discharge occurs, some of the charge stored by the coverglass is lost. Experimentally, coverglass potential drops during discharges of up to several hundred volts from the steady state value have been observed²⁸. Before the next arc can occur at the same location, the dielectric must restore some, or all, of the lost charge. It is assumed that the dielectric restores its lost charge through bombardment by the ambient ions since the electric field at the triple junction drops after the discharge and the field emission ceases to charge the dielectric. Once the dielectric charge is recovered so that the electric field induces a significant amount of field emission current, the EFEE charging resumes and results in the next discharge.

For large solar arrays, it can be assumed that arcing can happen independently at separate locations on the array. That is, arcs at one location do not affect the charging processes at sites distant from the arc site. Sites widely separated are thus said to be uncorrelated. The area of correlation is taken to be the area of the discharge wave created by an arc. This area is taken to be $0.012m^2$ based on experimental measurements in Reference 11. For the simulations, the array area is divided into correlated areas and the arc rates are determined independently for each area. The total arc rate for the array is then taken to be the sum of the rates for the correlated areas.

The time between arcs, τ_{arc} is the minimum charging time of all the sites on the interconnector within the correlated area, given by

$$\tau_{arc} = \min(\tau_{ion} + \tau_{fee}), \quad (8)$$

where τ_{ion} is the ambient ion charging time and τ_{fee} is the enhanced field electron emission charging time. Numerical results showed that the critical condition for arcing onset after

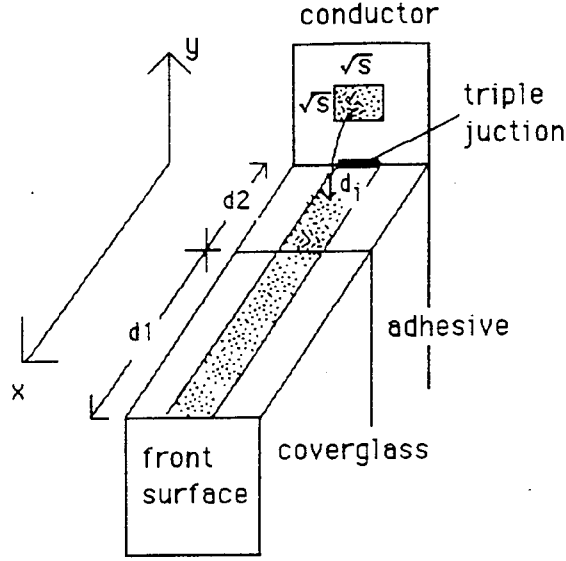


Figure 4: Geometry for EFEE charging

EFEE charging has been initiated is whether the desorbed neutral density is larger than the critical value of approximately $6 \times 10^{21} m^{-3}$. If the neutral density is above this value, breakdown occurs. If the density is below this value, the electron current just becomes space charge limited and eventually relaxes without leading to breakdown. In this case, a very short current pulse would be seen, without an arc flash or arc damage. Current pulses such as these, with timescales on the order of a nanosecond, have been detected in many experiments. In previous work by Mong and Hastings²², it was assumed that the neutral density was always above the critical value, resulting in an upper bound for the breakdown discharges. The next chapter will discuss how the neutral density criterion was incorporated into the simulations.

2.1 EFEE Charging Time

The geometry considered for EFEE charging is shown in Figure 4.

The rate of change of the electric field at the emission site on the conductor is given by

$$\frac{dE_e}{dt} = \eta \xi \frac{(\gamma_{ee} - 1) \sqrt{S_{real}}}{C_{diele} d_i^2} A' \beta^2 E_e^2 \exp\left(-\frac{B}{\beta E_e}\right). \quad (9)$$

For a detailed derivation of this relation, the reader is referred to Reference 3. The factor η , which was introduced to compensate for the difference in the value of the electric field at the emission site to that at the triple junction, is calculated from the following polynomial

fit determined from the numerical schemes

$$\eta = 1 + \sum_{n=1}^{n=4} a_n ((\bar{y} - 1)^{2n} - 1), \quad (10)$$

where $\bar{y} = y/(d_{gap}/2)$, y is the distance of the emission site from the triple junction, and d_{gap} is the interconnector length. The factor ξ is introduced to account for the discontinuity of the electric field due to the difference in the dielectric constants of the adhesive and coverglass. If the first impact point of the emitted electrons on the dielectric surface is within the adhesive, i.e. $d_i < d_2$, then ξ is unity. If the impact point is within the coverglass, then ξ is given by

$$\xi = \left[\frac{d_2}{d_i} + \frac{\epsilon_{d_2}}{\epsilon_{d_1}} \frac{(d_i - d_2)}{d_i} \right]^{-1}. \quad (11)$$

ξ_0 is the value of ξ with $d_i = d_1 + d_2$. The first impact point is also calculated from a polynomial fit to numerical results given by

$$\frac{d_i}{d} = \sum_{n=1}^{n=4} b_n \left(\frac{y}{d} \right)^{\frac{1}{2n}} \quad (12)$$

where $d = d_1 + d_2$. The capacitance per unit area of the dielectric side surface, $C_{diele}(d_i)$ is determined from a fifth order polynomial fit to the results of a capacitance matrix scheme¹⁶ given by

$$\frac{C_{diele}(d_i)}{C_{norm}} = \frac{1}{\sum_{n=1}^{n=6} c_n \left(\frac{d_i}{d} \right)^{n-1}} \quad (13)$$

where C_{norm} is the capacitance per unit area of the front surface

$$C_{norm} = \frac{1}{\frac{d_1}{\epsilon_{d_1}} + \frac{d_2}{\epsilon_{d_2}}} \quad (14)$$

The term γ_{ee} is the secondary electron yield given by Reference 9 as

$$\gamma_{ee} = \gamma_{max} \frac{E_i}{E_{max}} \exp \left(2 - 2 \sqrt{\frac{E_i}{E_{max}}} \right) \exp[2(1 - \cos \theta_i)]. \quad (15)$$

Here E_i is the incident energy of the emitted electrons impacting the dielectrics given by

$$E_i = e\phi_d = \frac{E_{TJ} d_i}{\xi} = \frac{\xi_0}{\xi} V \frac{d_i}{d} \quad (16)$$

and θ_i is the incident angle of those electrons at the first impact site given by

$$\theta_i = \arctan \left(\frac{d_i}{y} \right). \quad (17)$$

In Eq. (15), γ_{max} is the maximum secondary electron yield at normal incidence and E_{max} is the electron incident energy for the maximum secondary electron yield. In Eq. (9), A' is

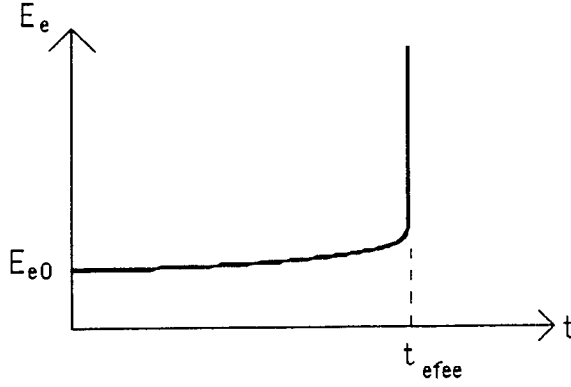


Figure 5: Typical Electric Field Run-Away

related to the Fowler-Nordheim coefficient A by

$$A' = \frac{S_{FN}}{S_{real}} \quad (18)$$

where the factor S_{FN}/S_{real} has been introduced to account for the negative space charge effect near the emission site. The term β in Eq. (9) is the electric field enhancement factor assigned to the emission site. This enhancement is due to manufacturing defects or impurities on the interconnector surface.

If the secondary electron yield is assumed to be constant, Eq. (9) can be integrated to obtain

$$E_e(t) = \frac{E_{e0}}{1 + \frac{\beta E_{e0}}{B} \ln \left(1 - \exp\left(-\frac{B}{\beta E_{e0}}\right) \left(\frac{B}{\beta}\right) C t \right)}, \quad (19)$$

where C is the constant given by

$$C = \eta \xi \frac{(\gamma_{ee} - 1) \sqrt{S_{real}}}{C_{diele} d_i^2} A' \beta^2 \quad (20)$$

and E_{e0} is the initial electric field at the electron emission site on the interconnector. Chapter 3 will discuss the method using a non-constant secondary electron yield. The electric field $E_e(t)$ has the characteristic shape shown in Figure 5

The field shows a run-away at a time $t = \tau_{efee}$ when the denominator in Eq. (19) vanishes. Thus, the field emission electron charging time τ_{efee} is given by

$$\tau_{efee} = \frac{1 - \exp\left(-\frac{B}{\beta E_{e0}}\right)}{\exp\left(-\frac{B}{\beta E_{e0}}\right)} \left(\frac{B}{\beta}\right) C \quad (21)$$

$$\simeq \frac{\beta}{B} \exp\left(\frac{B}{\beta E_{e0}}\right) \frac{1}{C} \quad (22)$$

$$= \frac{C_{diele} d_i^2}{(\gamma_{ee} - 1) \sqrt{S_{real}} \eta \xi A \frac{S_{FN}}{S_{real}} B \beta} \exp\left(\frac{B}{\beta E_{e0}}\right). \quad (23)$$

The initial electric field at the emission site E_{e_o} can be expressed in terms of the potential difference between the coverglass front surface and the triple junction as

$$E_{e_o} = \eta \frac{V}{d} \xi_0. \quad (24)$$

Thus, τ_{efee} is given by

$$\tau_{efee}(V) = \frac{C_{diele} d_i^2}{(\gamma_{ee} - 1) \sqrt{S_{real}} \eta \xi A' B \beta} \exp\left(\frac{Bd}{\beta \eta \xi_0 V}\right). \quad (25)$$

The implicit assumption in this analysis is that the secondary electron yield is greater than unity. If the yield is less than unity, positive charging of the dielectric side surface will not occur and the field will not run away.

2.2 Ion Charging Time

The calculation of the ion charging time is simpler than that for the EFEE charging time. If an arc occurs when the potential difference between the front surface and conductor is V_a and the coverglass front surface loses charge ΔQ , then the potential difference drops to $V_a - \Delta Q/C_{front}$, where C_{front} is capacitance of the front surface given by

$$C_{front} = \frac{1}{(A_{cell} \epsilon_{d_1})/d_1 + (A_{cell} \epsilon_{d_2})/d_2}. \quad (26)$$

The ambient ion charging time for the voltage to recover to the value V_e is then given by

$$\tau_{ion} = \frac{[V_e - (V_a - \frac{\Delta Q}{C_{front}})] C_{front}}{en_e v_{ion} A_{cell}} \quad (27)$$

where $en_e v_{ion}$ is the ion flux to the coverglass front surface of area A_{cell} . This gives a total charging time of

$$\tau_{chrg} = \frac{(V_e - (V_{arc} - \frac{\Delta Q}{C_{front}})) C_{front}}{en_e v_{ion} A_{cell}} + \frac{C_{diele} d_i^2}{(\gamma_{ee} - 1) \sqrt{S_{real}} \eta \xi A \frac{S_{FN}}{S_{real}} B \beta} \exp\left(\frac{Bd}{\beta \eta \xi_0 V_e}\right) \quad (28)$$

2.3 Arc Rate Code

Using the model above, a computer code was written by Cho³ to determine the arc rate for high voltage solar cells operating in a plasma environment. A slightly modified version of this code, which neglected the effects of neutral density on the arc rate, was used by Mong and Hastings to predict arc rates for the PASP Plus experiment. A description of this program will be given here, while the next chapter will discuss modifications made to the code. A flow chart of the code written by Cho is shown in Figure 6.

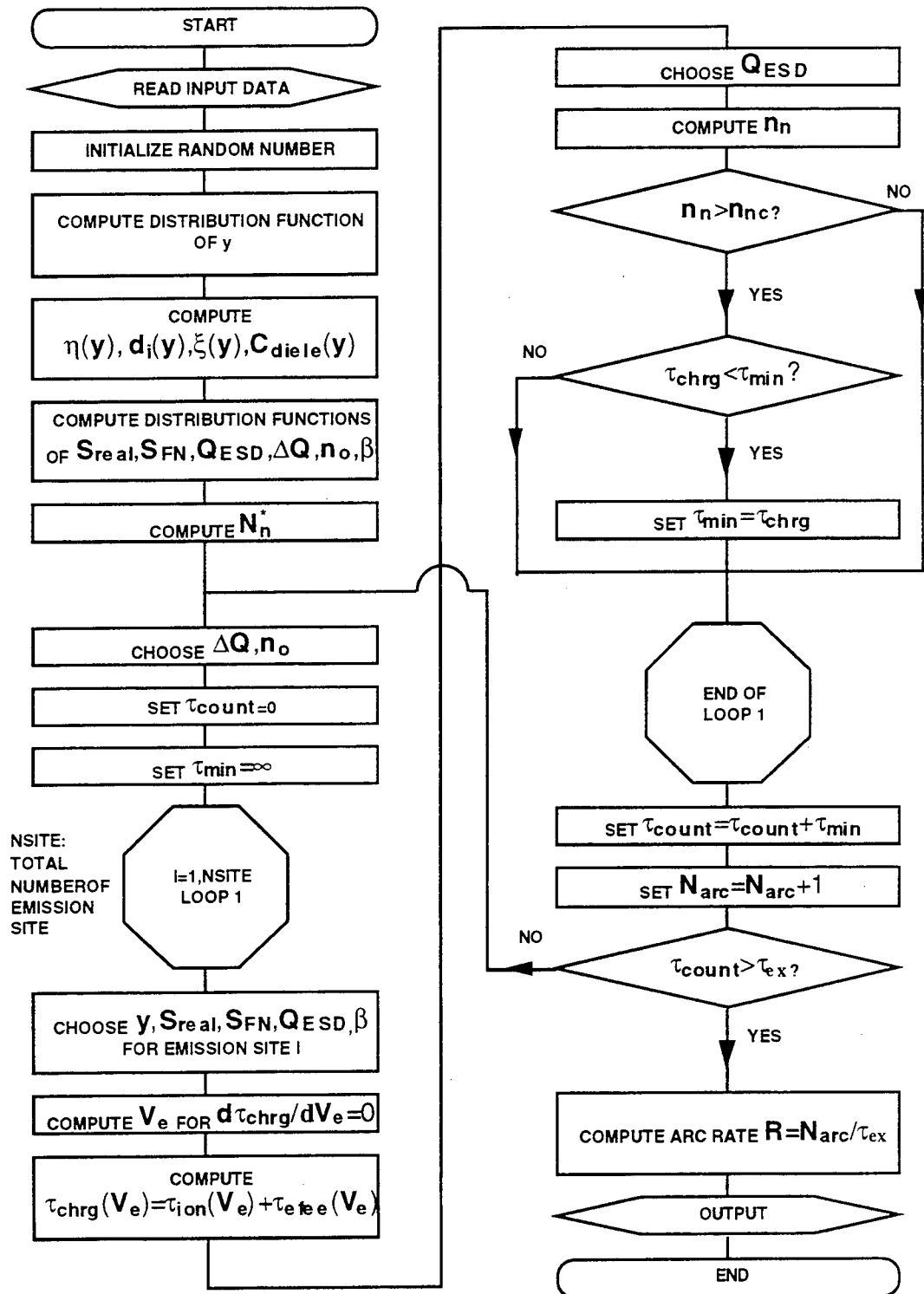


Figure 6: Flow Chart of Semi-Analytic Arc Rate Code

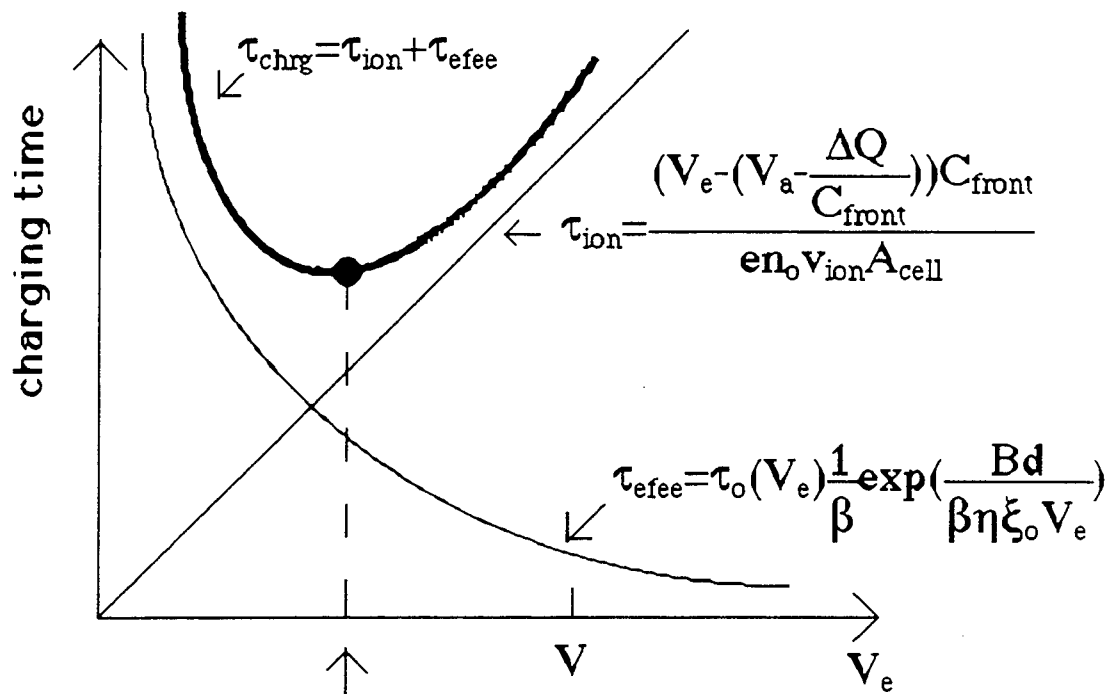
The program first reads in the input data. This includes the information about the cell dimensions and materials, the experimental parameters (i.e. bias voltage, experiment duration, cell temperature, environmental parameters, etc.), as well as the ranges of the parameters S_{real} , S_{FN} , ΔQ , etc. The emission site density is read in at this point, which will set the number of sites on the conductor. The array is then divided into correlated areas based on the discharge wave area.

Next, the distributions of η , ξ , d_i , and C_{diele} are calculated using Eq. (10) - (13). Uniform distributions of S_{real} , S_{FN} , and the electron stimulated desorption cross section Q_{ESD} in $\log_{10} S_{real}$, $\log_{10} S_{FN}$, and $\log_{10} Q_{ESD}$ are calculated between minimum and maximum values read in from the input data. The distribution of $\Delta - Q$ is calculated as a linear distribution between minimum and maximum values. The distribution of the field enhancement factor β is calculated from $f(\beta) = f_0 \exp(-\beta/\beta_0)$, where f_0 is a constant determined from the normalization condition $\int f(\beta) d\beta = 1$ and β_0 is a constant which determines the shape of the distribution.

Next, the code loops through the correlated areas. For each area, a loop is made through the emission sites within the area. All the parameters needed for Eq. (28) are then chosen randomly from the distributions previously calculated or determined using the equations listed above. To determine the charging time for the site using Eq. (28), the term V_e needs to be determined. This is the potential difference between the coverglass and the conductor when the EFEE charging is initiated. It is not necessarily equal to the bias voltage. This is due to the fact that after an arc occurs, as the dielectric recovers its lost charge through ion charging and the electric field at the conductor begins to increase, EFEE charging can start as soon as the conductor surface feels a strong enough electric field. Therefore, the voltage V_e is found by finding the minimum of Eq. (28), which assumes that the secondary electron yield is constant (see Figure 7). This is done by solving the differential equation

$$\frac{d\tau_{arc}}{dV_e} = 0 \quad (29)$$

using a Newton-Raphson scheme. The arcing time for the site is then calculated using this value of V_e . This is done for each site in the correlated area, and the site with the minimum charging time is the one that arcs. An arc counter is then incremented and the charging time is added to a running timer. The process is then repeated until the timer exceeds the experiment duration. The arc rate is then found by summing the arc counts from all the correlated areas and dividing by the experiment duration.



EFEE charging begins when the voltage between the triple junction and the cover-glass front surface recovers to this value.

Figure 7: Minimum Charging Time

Chapter 3

Modifications to Semi-Analytic Arc Rate Code

In the previous chapter, the arc rate code developed by Cho and Hastings was described. This chapter will discuss modifications made to this code to make it more physically accurate and to allow it to accurately model the PASP Plus experiment as the satellite moves through the changing environment of its orbit. A flow chart of the modified code is shown in Figure 8.

The code now has a driver at the front end of the program. This allows the environmental parameters to be defined at one second intervals during the experiment. Thus, when simulating arcing on orbiting spacecraft, the environmental data for the orbit can be set at one second intervals based on either actual data or data generated using environmental models. The bias voltage, experiment time, and cell type are also set in the driver. Output files are then opened. Data from the arc rate simulation can be dumped to these files for one second intervals during the experiment. This was done to match the format of the data for the PASP Plus experiment. This information is then passed to the *arcrate* subroutine.

The cell data, consisting of cell dimensions and material properties are then read in. Next, the distributions of η , d_i , ξ , C_{diele} , S_{real} , S_{FN} , Q_{ESD} , and β are calculated as before. The distribution of the amount of charge lost from an arc, ΔQ , is now a linear distribution of the percent of charge stored by the dielectric instead of a distribution between two fixed values. The array is then divided into correlated areas based on the discharge wave area.

The code then loops through these correlated areas. The occurrence of a breakdown discharge at a site in an area will reset the charging process of all other emission sites within that area, but will not affect the charging at sites in the other areas. However, as discussed in Chapter 2, if the neutral density at a site is not greater than the critical neutral density, breakdown will not occur. A small current pulse, hereafter referred to as a "small arc" will be generated, but no discharge wave will be created. Thus, the charging at the other sites

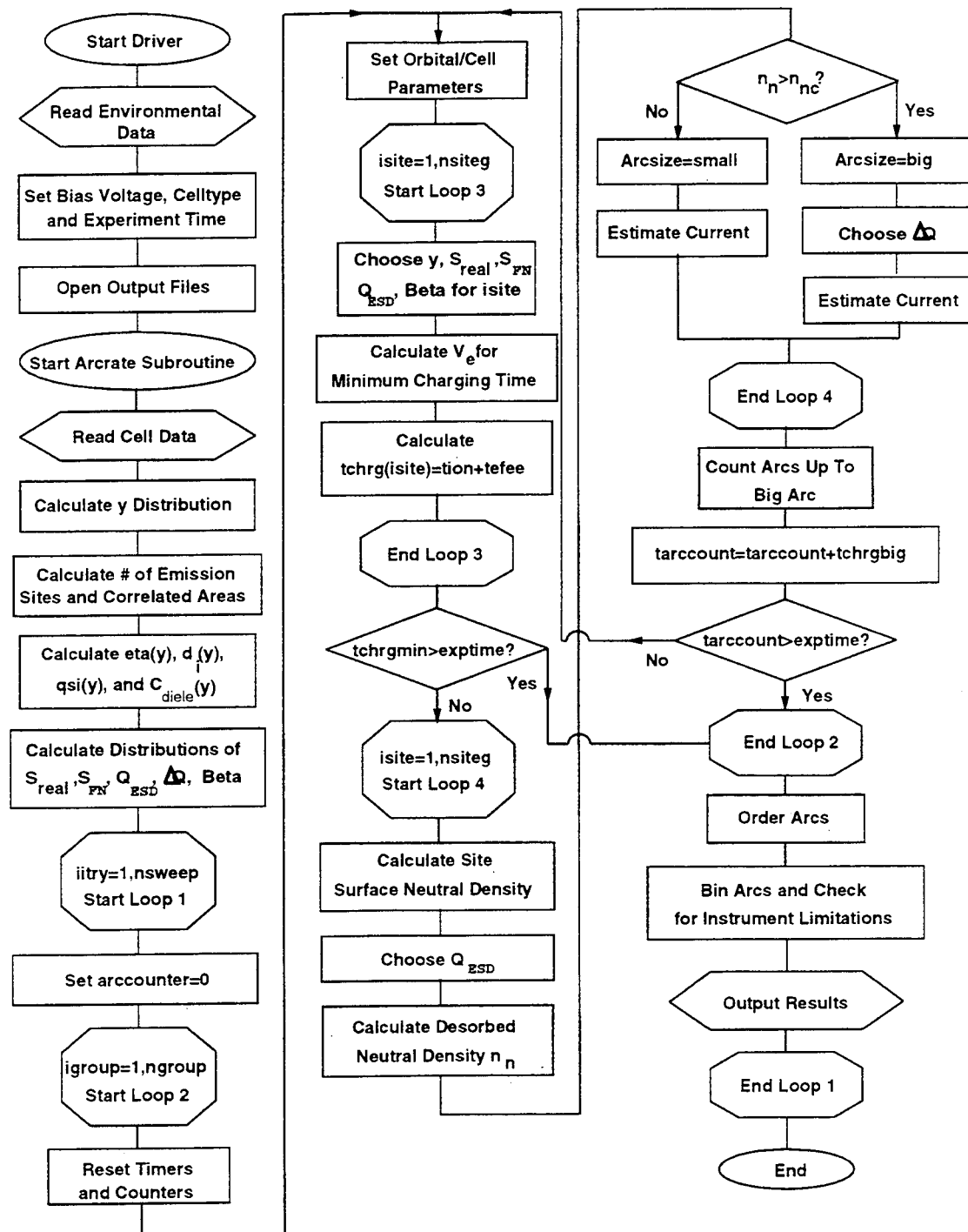


Figure 8: Flow Chart of Modified Arc Rate Code

will continue until one of the sites experiences breakdown ("big arc"). Previously, either the small arcs were ignored and only the big arcs were counted, or, as in the work done by Mong and Hastings²², the neutral density criterion was ignored, resulting breakdown in every case. Now, both big and small arcs are counted, with the sum giving the total arc rate. The results from numerical simulations showed that the current seen from a small arc is on the order of microamps to a few milliamps. Big arcs are typically current pulses on the order of amps. An input current threshold was added to the code to screen out arcs that would be below the level detectable by equipment used in an experiment. For example, the recently flown shuttle based SAMPIE experiment had a detectable current threshold of 100 mA. Thus, only big arcs would be seen by this experiment.

The charging time for each emission site within the correlated area is then calculated. In previous work by Cho³ and then by Mong²², the secondary electron yield of the dielectric was assumed to be constant. This allowed Eq. (9) to be integrated, resulting in a closed form solution for the EFEE charging time given by Eq. (25). The assumption that the secondary electron yield is constant, however, is not physically accurate. As the electric field builds up, the emitted electrons are accelerated to a higher velocity before striking the dielectric surface. This increased velocity results in a higher secondary electron yield. Thus, the secondary electron yield will increase as the EFEE charging takes place. When the equation for the secondary electron yield as a function of the electric field, Eq. (15), is inserted in Eq. (9), a non-linear differential equation results, which can not be solved in a closed form as was possible for the case when the secondary electron yield was assumed to be constant. Thus, the EFEE charging time must now be calculated numerically, using a Runge-Kutta scheme with adaptive stepping²⁶. The total charging time for the emission site τ_{chrg} is determined by numerically finding the minimum of

$$\tau_{chrg} = \tau_{ion} + \tau_{efee} \quad (30)$$

where τ_{ion} is given by Eq. (27) and τ_{efee} is found by numerically integrating Eq. (9) with the boundary conditions

$$E_{e_{initial}} = \frac{\eta \xi_0 V_e}{d_1 + d_2} \quad (31)$$

and

$$E_{e_{final}} = 2E_{e_{initial}}. \quad (32)$$

The choice of the final boundary condition comes from the fact that the field runaway follows the characteristic shape shown in Figure 5, where the field remains almost constant until the runaway time.

Once the charging time has been calculated for all the emission sites, the breakdown criterion must be judged. To do this, the desorbed neutral density n_n at the site is compared to the critical neutral density n_{nc} , which was determined by Cho³ to be approximately $6 \times 10^{21} m^{-3}$. The desorbed neutral density is given by Reference 3 as

$$n_n = 2.08 \frac{N_n Q_{ESD}}{\bar{c}} \frac{\epsilon_0}{e} \sqrt{\frac{2e}{m_e}} \frac{\sqrt{E_{se}}}{E_{se1} d^2} \|V_e\|^2 \quad (33)$$

where N_n is the adsorbed neutral density on the dielectric surface before the intensive outgassing due to the EFEE begins, ϵ_0 is the dielectric constant of vacuum, e is the electron charge, m_e is the electron mass, E_{se} is the secondary electron emission energy in eV, E_{se1} is the energy for a secondary electron yield of unity, $d = d_1 + d_2$, and \bar{c} is the average speed of the desorbed neutrals, which are assumed to be at the temperature of the dielectric surface T_s , so that

$$\bar{c} = \sqrt{\frac{8\kappa T_s}{\pi m_n}} \quad (34)$$

where m_n is the mass of the neutrals which are assumed to be water. In the previous work by Cho, the adsorbed neutral density N_n was assumed to be at the steady-state value determined by the balance of the thermal stimulated desorption of neutrals to the flux of ambient neutrals onto the dielectric surface, found by solving the following equation for $N - n$

$$k_1^0 N_n \exp\left(-\frac{E_d}{\kappa T_s}\right) = n_{na} \frac{\bar{c}}{4} \left(1 - \frac{N_n}{N_{n0}}\right), \quad (35)$$

where k_1^0 is the neutral thermal desorption coefficient, E_d is the adsorption energy, n_{na} is the ambient neutral density, and N_{n0} is the neutral surface density for monolayer coverage of the surface. The term $1 - N_n/N_{n0}$ is an approximation for the probability that a neutral striking the surface will stick. The flux of neutrals onto the surface was assumed to be only due to the thermal flux of ambient neutrals.

In this research, however, the steady-state surface neutral density is not assumed, since an arc could occur at a site before the steady state could be reached. Therefore, the change in the surface neutral density with time is given by the difference between the flux of the neutrals from the surface and the flux of neutrals onto the surface that stick

$$\frac{dN_n}{dt} = \left(\Gamma_n + n_{na} \frac{\bar{c}}{4}\right) \left(1 - \frac{N_n}{N_{n0}}\right) - k_1^0 N_n \exp\left(-\frac{E_D}{\kappa T_s}\right), \quad (36)$$

where Γ_n is the component of the neutral flux onto the side surface due to the orbital velocity

$$\Gamma_n = n_{na} v_{orbit} \cos \alpha, \quad (37)$$

with v_{orbit} being the orbital velocity and α the angle of attack of the arrays to the ram (an angle of attack of 90 corresponds to the spacecraft velocity vector and the vector normal to

the array front surface being parallel). The surface neutral density, as a function of time, is therefore given by

$$N_n(t) = \frac{C_1}{C_2} (1 - e^{-C_2 t}) \quad (38)$$

where C_1 and C_2 are given by

$$C_1 = \Gamma_n + n_{na} \frac{\bar{c}}{4} \quad (39)$$

$$C_2 = \frac{C_1}{N_{n0}} + k_1^0 N_n \exp\left(-\frac{E_D}{\kappa T_s}\right). \quad (40)$$

The surface neutral density at the time of the arc is calculated from Eq. (38) with the time set to the difference between the time of the arc and the time of the previous arc at that site. This time is the time for which the neutrals have been recharging the surface. If there was no previous arc at the site, the recharging time was set to 1×10^{30} , resulting in the steady state surface neutral density. The ambient neutral density n_{na} was taken to be 100 times the actual ambient density based on numerical work by Cho³ which found that the neutral gas pressure over the solar cell after an arc was as high as 20 torr when the background density was on the order $< 10^{-3}$ torr.

From Eq. (38) and (33), it can be seen that the desorbed neutral density is a function of the ambient neutral density, cell temperature, voltage, and electron stimulated desorption cross section Q_{ESD} . Thus, for a given voltage and value of Q_{ESD} , the ambient density needed to result in the desorbed neutral density exceeding the critical density can be determined for various cell temperatures. Figure 9 shows the critical ambient neutral density needed for breakdown at a voltage of -500V and a Q_{ESD} of $1 \times 10^{-19} m^2$. As can be seen, the ambient neutral density needed to allow breakdown is a strong function of temperature. Conversely, the cell temperature needed to allow a sufficiently large surface neutral density to lead to breakdown can be seen to be a function of ambient neutral density, as well as of voltage and Q_{ESD} . The surface of critical ambient neutral density versus temperature and voltage is shown in Figure 10.

When the solar cells are cold and there is a high ambient neutral density, there is a higher surface neutral density, and therefore a higher desorbed neutral density, which results in a larger probability of breakdown, and thus a larger arc rate. In the limit, all of the possible arcs will have a desorbed neutral density greater than the critical density and will result in breakdown. This is the limit used in the earlier work by Mong²². However, when the cells are warm and/or the ambient neutral density is low, many, or all, of the possible arcs will not have a sufficiently large desorbed neutral density to allow breakdown to occur, resulting in a lower arc rate.

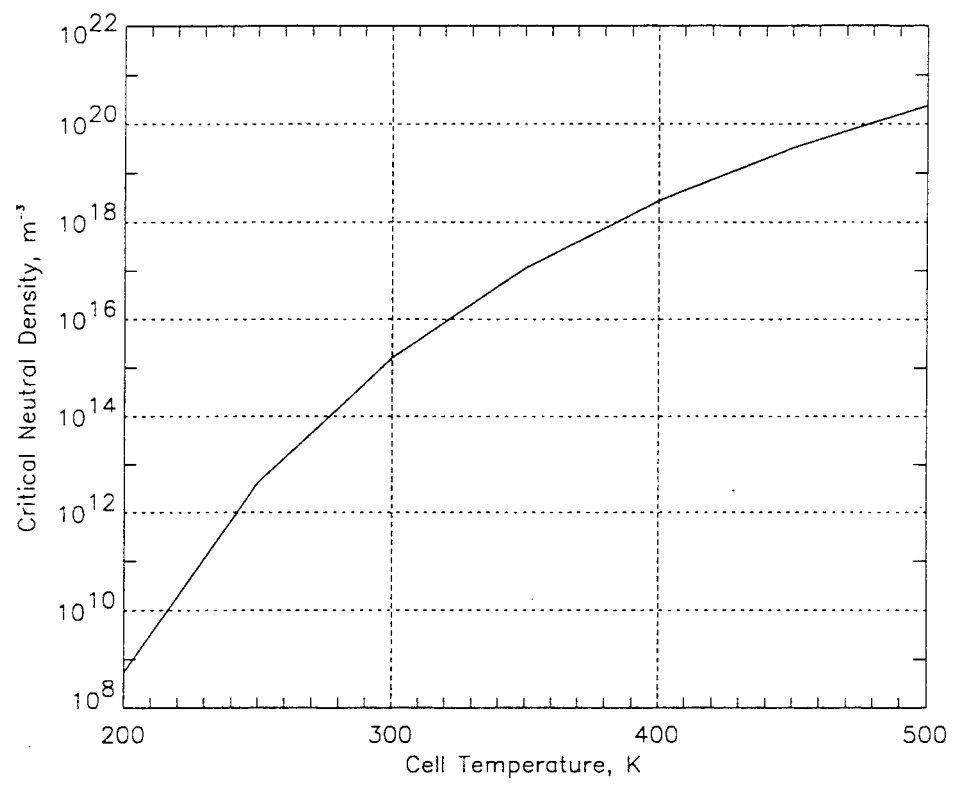


Figure 9: Critical Ambient Neutral Density Variation with Temperature

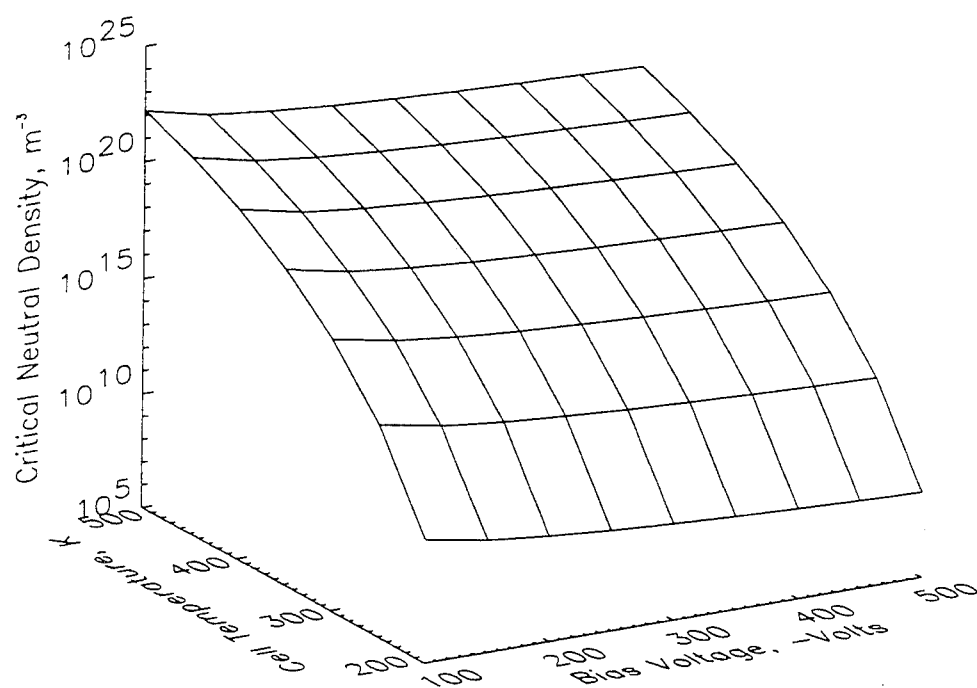


Figure 10: Critical Ambient Neutral Density Variation with Temperature and Voltage

Once the surface neutral density at the site is known, a value for Q_{ESD} is randomly chosen from the distribution of Q_{ESD} and the desorbed neutral density is calculated using Eq. (33). This is then compared to the critical neutral density to determine if breakdown occurs (i.e., whether a small or big arc occurs at the site). After the arc size has been determined for all the sites within the correlated area, along with the time of the arcs, all the small arcs up to the first big arc are counted, along with the big arc. Since this big arc resets the charging process at all the sites within the correlated area, the big arcs that would have occurred after this first big arc are disregarded and the process is repeated until the time exceeds the experiment duration.

The arcs from all the correlated areas are then summed to give the total arc counts. The code has also been modified to be able to include arc count limitations within the experimental equipment. For example, the PASP Plus transient pulse monitors have an upper limit of fifteen arcs per second. The final simulated results are then output after screening for arc current and arc rate limitations within the experimental equipment.

This semi-analytic arc rate code can be used to predict the arcing activity of conventional geometry cells in a plasma environment. In the next chapter, the results of predictions using this code for the PASP Plus experiment will be discussed. The code was also recently used to predict the arcing on the SAMPIE experiment, with experimental values falling either within or very near the predicted values.

Chapter 4

PASP Plus Predictions

In March, 1994, the Solar Array Module Plasma Interactions Experiment (SAMPIE) was flown aboard the Space Shuttle. In the next few years, three more space missions are planned to study high voltage solar arrays, including the Photovoltaic Array Space Power Plus Diagnostics (PASP Plus) experiment. By using the semi-analytical model discussed in the previous chapter for the conventional cells, arcing predictions were made for the PASP Plus mission to aid in its preparation and to further check the validity of the model.

4.1 PASP Plus

The Air Force anticipates that future missions will require more survivable, higher powered space systems. This requirement demands more efficient, survivable, and radiation hardened solar array systems operating at higher voltages to minimize the mass requirements and resistive losses in the power distribution subsystem. The interactions of these high voltage arrays with the space plasma and radiation environments need to be clearly understood in order to improve the reliability of the future systems. Because of the complex nature of these interactions, ground simulations are inadequate to accurately quantify the effects of the space environment on the solar array systems. Thus, the PASP Plus experiment was designed to gather a large base of flight test data to be used to develop an understanding of the interaction of both highly positive and negative biased solar arrays. PASP Plus has four main objectives²⁴:

- (1) Characterize the electrical performance and environmental interaction of a set of advanced solar arrays operating at high voltages in the natural space environment.
- (2) Characterize the long-term radiation degradation effects of several advanced solar arrays operating in a harsh space radiation environment.
- (3) Determine an environmental cause-and-effect relationship for the impact of the space environment on the operation of solar arrays.

- (4) Obtain flight performance data for advanced array designs never before flown.

4.2 Hardware Description

The PASP Plus is the primary experiment on the Advanced Photovoltaic and Electronics Experiments (APEX) satellite. This satellite is part of the Space Test Program (STP) of the Air Force's Space and Missile Systems Center. Two other radiation effects on electronics experiments, CRUX and FERRO, will also be flown on the APEX satellite. The satellite, built by the Orbital Science Corporation, is scheduled to be placed into a 360 x 1950 km, 70° inclination orbit via Pegasus launch vehicle in the summer of 1994. This elliptical polar orbit will allow the spacecraft to operate in a broad range of the space plasma, neutral, and radiation environments. The solar arrays on the spacecraft will be continuously sun pointing, resulting in operation at various angles of attack in both the ram and wake. The experiment is expected to operate for one to three years.

The deployed configuration of the APEX satellite is shown in Figure 11. The solar arrays to be tested are located on the top shelf of the body and on one of the deployed panels. The other three panels are the solar arrays used to generate the power for the spacecraft operation. Most of the diagnostic equipment is located on the avionics shelf located under the payload shelf.

4.2.1 Diagnostic Equipment Description

Diagnostic sensors for the PASP Plus experiment include²⁷:

- (1) Sun sensor to measure the incident angle of the solar energy.
- (2) Langmuir probe to measure the plasma temperature and density. The probe will also have a potential sensor (SENPOT) to sense and compensate for the vehicle frame potential, which may be more negative than the space plasma potential.
- (3) Four remote E/M discharge sensors connected to a transient pulse monitor to detect and fully characterize (amplitude, rise time, integral, and number of pulses per second) the arc discharges that occur during the negative biasing portion of the experiment. These monitors have a rate limitation of 15 arcs/second.
- (4) Electrostatic analyzer to measure the 30 eV to 30 keV electron/ion spectra and detect the passage of the spacecraft through the auroral region.
- (5) Dosimeter to measure the short and long term ionizing particle (electron and ion) radiation dosage.

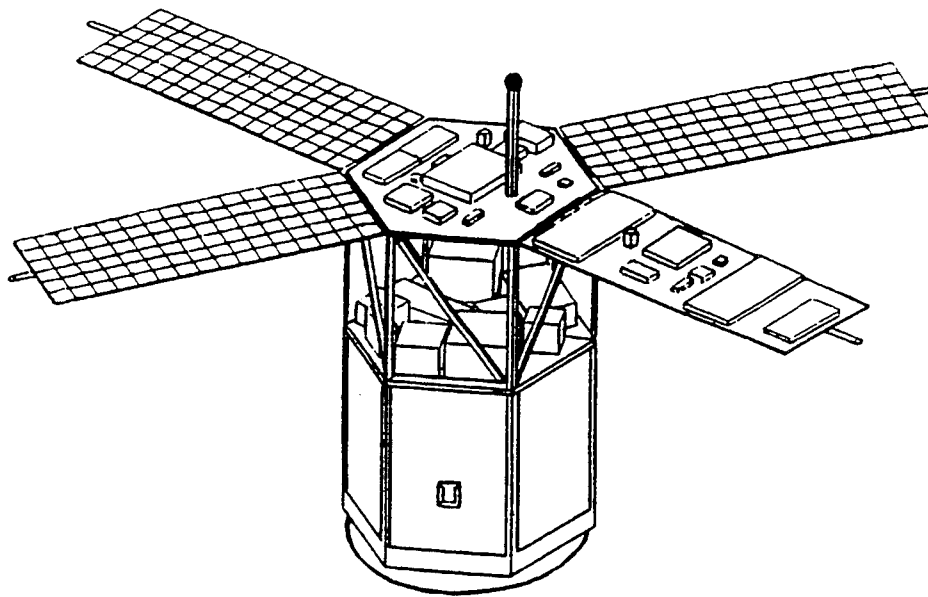


Figure 11: Deployed APEX Spacecraft with PASP Plus Experiment

(6) Contamination monitors to measure the amount and effect of molecular and particulate contamination on the array surfaces. Two types of monitors will be used. Quartz Crystal Microbalances (QCMs) will be used to measure the mass of contamination being deposited on the surface, while Thermal Coated Calorimeters will determine the optical degradation of the coverglass through α/ϵ measurements.

(7) Temperature sensors to measure the temperature of the arrays.

In addition, an electron emitter will be available to emit a stream of electrons to alter the spacecraft potential. This will allow the experiment to simulate more accurately the positive high-voltage operation of large functional arrays.

4.2.2 Solar Array Module Descriptions

There will be seventeen arrays of twelve different types flown on the payload shelf and deployed panel of the spacecraft. Since there are only sixteen electrical channels, one of the arrays will not be used. Ten of these arrays will be subject to voltage biasing. The information for these arrays are taken from References 22 and 1. The array modules are numbered from 0 to 15 for identification. Arrays #0, #1 and #2 are conventional silicon solar cells. Module #3 is made up of silicon wrap-through-contact (WTC) cells designed

for Space Station Freedom (SSF). Arrays #4 and #6 are Applied Solar Energy Corporation's (ASEC) gallium arsenide/germanium (GaAs/Ge) conventional cells. TRW's APSA cells make up array #5 (previously labeled array #36). The advanced solar cells of AlGaAs/GaAs Monolithic MBG are on array #7. Array #8 is made of Spectrolab's GaAs/Ge WTC cells. Amorphous silicon cells developed by TRW and Solarex are located in module #9. Array #10 contains advanced indium phosphate (InP) cells. Spectrolab's conventional GaAs/Ge cells are in array #11. Modules #12 and #13 are made up of Boeing's GaAs/CuInSe MBG cells. Two concentrator designs are being flown in modules #14 and #15. Module #14 is the Mini-Cassegrainian GaAs cell from TRW, while module #15 contains the Boeing Mini-Dome Fresnel Concentrator. Of these, modules #1, 2, 3, 4, 5, 6, 8, 11, 14, and 15 are the arrays subject to high voltage biasing. Predictions will be presented here for the conventional geometry cells (arrays #1, 2, 4, 5, 6, and 11).

The biased conventional silicon cell arrays #1 and #2 are representative of virtually all of the arrays flying on DoD, NASA, and commercial spacecraft today. The cells were manufactured by Spectrolab Inc. and incorporated into an array by RCA in 1984. In addition to the objectives stated above, these cells will also be compared to the well documented degradation characteristics of Si to insure the accuracy of the dosimeter readings. The silicon cells are $2\text{cm} \times 4\text{cm}$ and $203\mu\text{m}$ thick. The coverglass is fused silica bonded to the cell with Dow Corning adhesive DC-93500, with estimated thicknesses of $153\mu\text{m}$ and $37\mu\text{m}$, respectively. The interconnector is assumed to be Kovar with an estimated work function of 4.76 eV. Array #1 contains twenty cells in series, while array #2 has sixty cells contained in three strings of twenty. Thus, differences in the arc rates between these arrays will help give the relationship between arcing and the number of cells.

A much thinner silicon cell design is being tested by the TRW Advanced Photovoltaic Solar Array (APSA) cells in module #5. The thin cells hold a large promise for future use due to mass cost savings they yield. The cells are $2.6\text{cm} \times 5.1\text{cm}$ with a thickness of only $63.5\mu\text{m}$ (2.5 mil) thick. More importantly for arcing considerations, the CMX coverglass thickness is only $51\mu\text{m}$ (2 mil) and the DC-93500 adhesive is estimated to be $76\mu\text{m}$ (3 mil) thick. The interconnector is silver plated invar, so the relevant work function is that of silver, which is 4.26 eV. The module is made up of twelve APSA cells. Examination of the arc rate of these cells will give insight into the relationship between arcing and cell thickness for silicon cells.

Modules #4 and #6 contain thin GaAs/Ge cells, which high efficiency, radiation resistant cells produced by the Applied Solar Energy Corporation. These contain $4\text{cm} \times 4\text{cm}$, $76\mu\text{m}$ (3.5 mil) cells with $102\mu\text{m}$ (6 mil) thick CMX coverglasses. The adhesive thickness is

Table 1: PASP Plus Cell Data

Instrument No.	1, 2	3	4, 6	8	11	5 (36)
Cell Type	Si	Si WTC	GaAs/Ge	GaAs/Ge WTC	GaAs/Ge	APSA
Manufacturer	RCA	NASA	ASEC	Spectrolab	Spectrolab	TRW
Cell Size (cm ²)	2x4	8x8	4x4	4x4	4x4	2.6x5.1
No. of Cells	20, 60	4	20, 12	4	8	12
Cell Gap (μm)	500	1000	500	1000	500	635
d_{cell} (μm)	203	203	89	178	178	56
d_1 (μm)	153	203	102	152	152	51
d_2 (μm)	37	N/A	51	N/A	76	76
ϵ_{d_1}	3.5	4	4	4	4	4
ϵ_{d_2}	2.7	3	2.7	3	2.7	2.7
γ_{max_1}	3.46	4	4	4	4	4
γ_{max_2}	3	2	3	2	3	3
E_{max_1} (eV)	330	400	400	400	400	400
E_{max_2} (eV)	300	200	300	200	300	300
ϕ_w (eV)	4.76	4.85	4.26	4.5	4.26	4.26

estimated to be $51\mu\text{m}$ thick. The interconnector is also silver plated invar. Array #4 contains four parallel strings of five cells, while array #6 has three parallel strings of four.

Module #11 has the thick GaAs/Ge (inactive Ge) cells made by Spectrolab Inc. These cells are $4\text{cm} \times 4\text{cm}$, $178\mu\text{m}$ (7 mil) thick, with $152\mu\text{m}$ (6 mil) thick coverglasses. The adhesive thickness is estimated to be $76\mu\text{m}$ (3 mil). There are two strings of four cells each in the module. By comparing the results from this module with modules #4 and #6, the relationship between arcing and cell thickness for the GaAs/Ge cells can be examined.

Table 1 summarizes the given and assumed cell properties for the conventional and wrap-through-contact cells that will be biased during the PASP Plus experiment.

4.3 Experiment Simulation

The PASP Plus arrays will be biased in sequences of four bias steps. Each bias step will last 23 seconds, with a 7-second interval for Langmuir probe sweeps and array I-V curves. Bias voltages between +500 volts and -500 volts are possible, though the APSA cells will not be biased beyond ~ 300 volts. In the simulations, however, the APSA cells were

Table 2: PASP Plus Bias Voltages

Seq No.	Step 0	Step 1	Step 2	Step 3
0	-	-	-	-
1	75	100	125	150
2	200	240	280	320
3	360	400	450	500
4	200	300	400	500
5	160	180	200	220
6	240	260	280	300
7	prog.	prog.	prog.	prog.

biased to -500 volts to allow comparison with the other arrays. During the experiment, the arrays to be biased can be selected, and will be biased in descending numerical order. The pre-programmed bias sequences are shown in Table 2, where sequence 0 is no biasing ("safe mode") and sequence 7 is programmable.

Predictions were made for the arcing of the conventional cells during the initial negative biasing phase of the experiment, hereafter referred to as Phase 1. In this phase of the experiment, the conventional cells will be biased on the odd days and the unconventional cells will be biased on the even days, following the schedule shown in Table 3. As stated earlier, predictions were made for the APSA cells even though they will not actually be biased beyond -300 volts. In this phase of the simulation, biasing will only be conducted from ± 20 minutes of the arrays being in ram during each orbit. The environmental data needed for the simulations was generated at one second intervals using the Environmental Workbench (EWB) software developed by S-Cubed. Temperature data for the cells was generated using a simple thermal model for the cells and spacecraft, along with data from Reference 23. Two sets of simulations were then run. In the first, the environmental parameters were first set to the maximum values from the generated environmental data, and the second used the minimum values. This was done to find the range of expected arc rates for the experiment, as well as to determine the expected probability of arcing. The second set of simulations used the generated data at one second intervals to actually simulate the experiment during the orbit.

Table 3: PASP Plus Phase 1 Biasing Sequencing

Seq No.	Step 0	Step 1	Step 2	Step 3
1 (Days 1,2)	-75	-100	-125	-150
5 (Days 3,4)	-160	-180	-200	-220
6 (Days 5,6)	-240	-260	-280	-300
3 (Days 7,8)	-360	-400	-450	-500

Table 4: Environmental Parameters for Minimum/Maximum Arcing

Condition	Plasma Density	Electron Temperature	Ion Mass	Ion Velocity	Neutral Density	Cell Temperature
Minimum	$2.8 \times 10^8 m^{-3}$	0.0715 eV	$2.21 \times 10^{-27} \text{kg}$	6536.79 m/s	$6.85 \times 10^9 m^{-3}$	285.0 K
Maximum	$3.5 \times 10^{11} m^{-3}$	0.347 eV	$2.64 \times 10^{-26} \text{kg}$	8083.78 m/s	$3.18 \times 10^{14} m^{-3}$	215.0 K

4.3.1 Arcing Ranges

A set of simulations were run to determine the expected arcing of the conventional geometry cells under the orbital conditions for maximum and minimum arcing. The parameters used are listed in Table 4.

In the simulations, 100 trials were run at each bias voltage for the two sets of conditions. The resulting range of arc rates for the conventional cells are shown in Figure 12. The upper curves show the maximum rates seen, while the lower curves show the minimum. For each cell, minimum rates of at or near zero arcs/second occurred for the entire voltage range, while the maximum rates varied from 0.56 to 4.3 arcs/second. The large area between the two curves represents the high anticipated scatter in the data. The thin cells (APSA and thin GaAs/Ge) showed the highest rates, as expected. The predictions for the silicon cells in modules #1 and #2 show that the arc rate will depend on the number of cells, which is expected since more cells results in a larger number of correlated areas in which arcs can occur independently. This is also evident by examining the rates from the two thin GaAs modules #4 and #6. In these simulations, as well as the second set of simulations conducted to represent the actual on-orbit experiment, it was found that at low cell temperatures, most of the arcs were "big arcs", while at high temperatures they were mostly, or solely, "small arcs". This is expected since at the high temperatures there is not a sufficient surface neutral density to be desorbed to lead to breakdown, whereas at low temperatures there is.

Table 5: PASP Plus Conventional Cell Onset Voltages

	Module 1	Module 2	Module 4	Module 5	Module 6	Module 11
Onset Voltage	-180	-180	-125	-125	-125	-200

Figure 13 show the range of probability of arcs occurring during the experiment. These probabilities are the percentage of trials in which at least one arc occurred. The upper curves show the probability of arcing under maximum conditions, while the lower curve shows the probability under minimum conditions. Thus, the actual probability of arcs occurring during the experiment lie between these curves, depending on the actual environmental conditions. During the actual experiment at voltages for which the probability is greater than zero but less than one, it is expected that arcing may occur in some trials and not in others. For a given bias voltage, it can be seen that the environmental conditions can greatly affect the chance of arcing. For example, at -500V the thick GaAs/Ge cells (module 11) experienced arcing in nearly 100 percent of the trials under maximum conditions, but arced in less than 60 percent of the trials under the minimum expected conditions. The thinner cells showed higher probabilities of arcing than the thick cells in addition to having higher arc rates.

By examining the results from the trials at maximum arcing conditions, expected onset voltages could be found. The voltages represent the level at which arcing was first seen to occur on the cells. Below these levels, no arcs occurred in any of the trials. The simulated arcing onset voltages for the cells are shown in Table 5

4.3.2 Orbital Simulation

The next set of simulations consisted of simulating the actual experimental operation of the PASP Plus conventional cells during Phase 1. Using the sequencing listed in Table 3, along with orbital data generated with EWB, the cells in the simulation were biased for ± 20 minutes of ram. With approximately thirteen orbits per day, this resulted in a database of approximately 1000 bias steps being conducted each day. Each of these step simulations, however, were done using the environmental data generated for the appropriate portion of the orbit. This database was then used to develop software using the Interactive Data Language from Research Systems, Inc. to be used to find correlations between arc rates and the various environmental and operational parameters.

For example, by scanning through the data for points of constant ion density, neutral density and cell temperature, a fit to the arc rate versus voltage similar to that found by

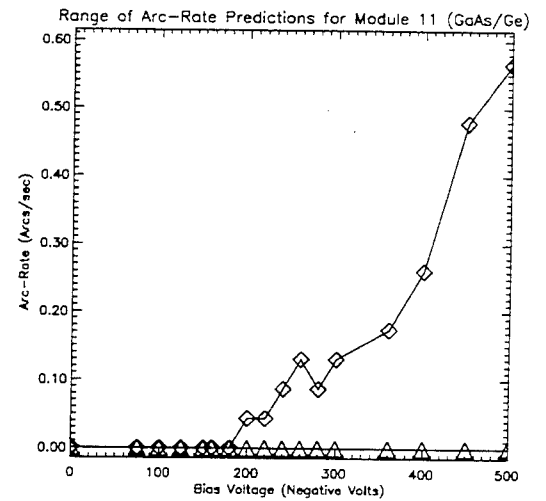
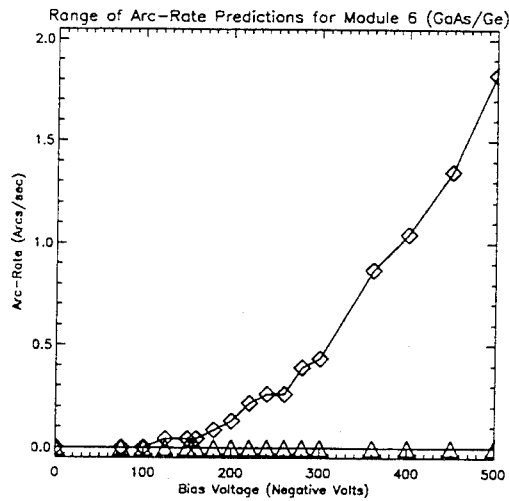
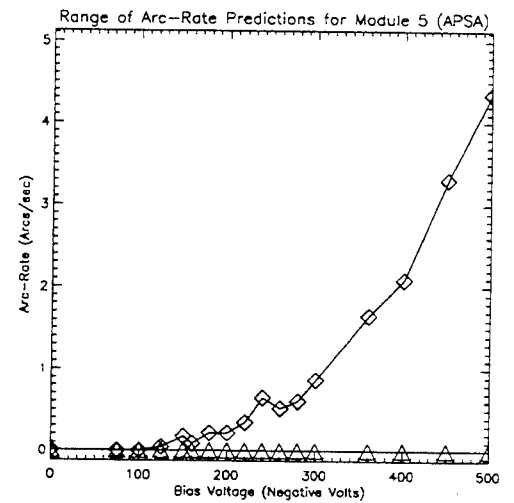
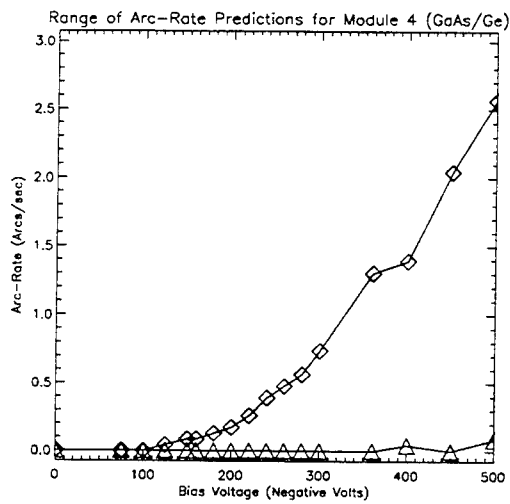
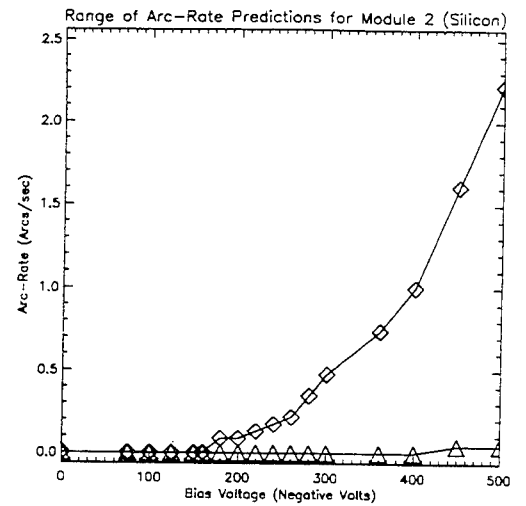
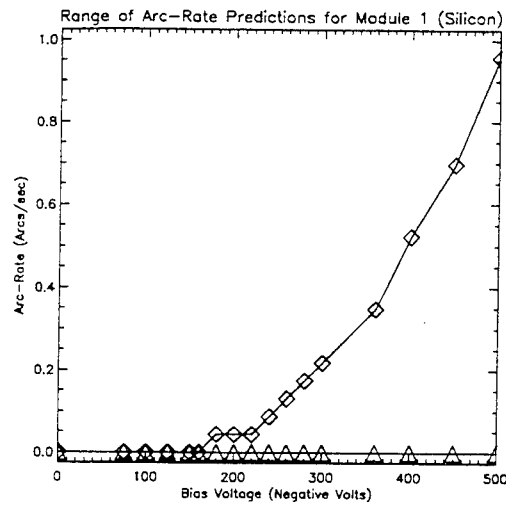


Figure 12: Range of Arc Rates for PASP Plus Conventional Cells

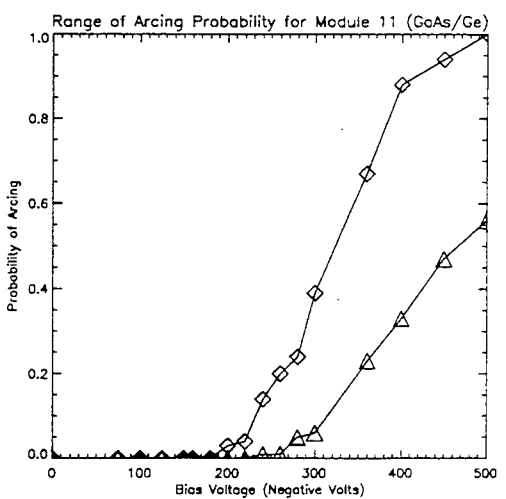
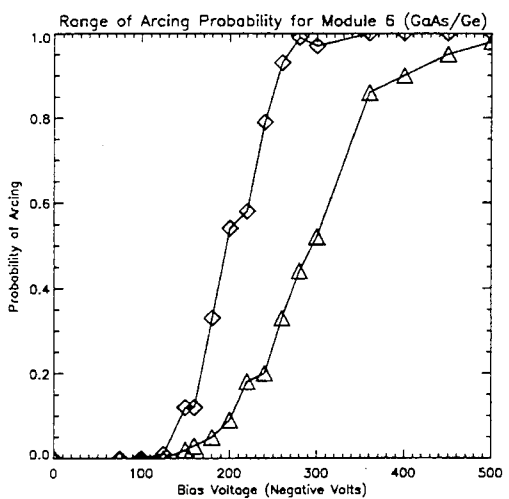
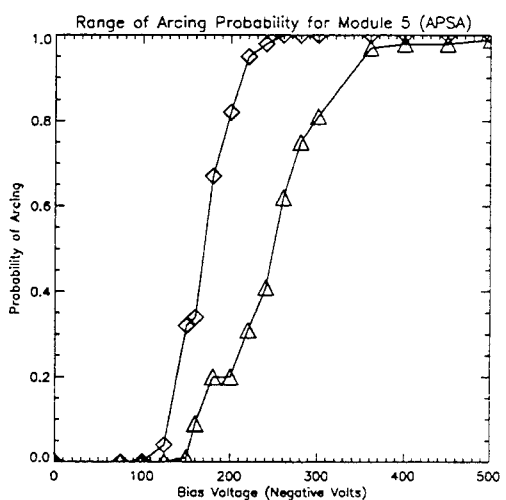
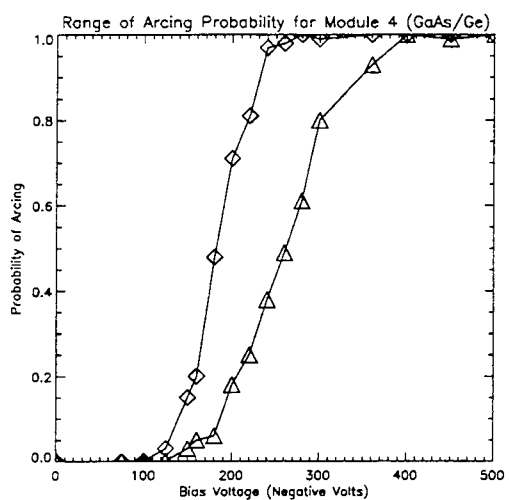
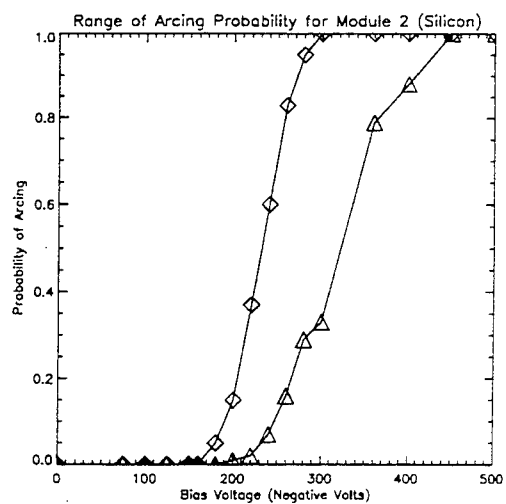
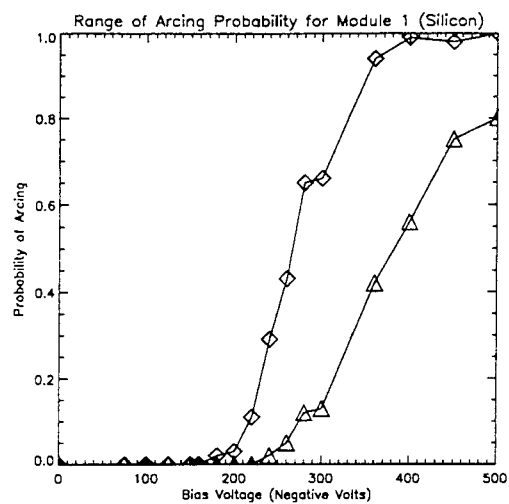


Figure 13: Range of Arcing Probability for PASP Plus Conventional Cells

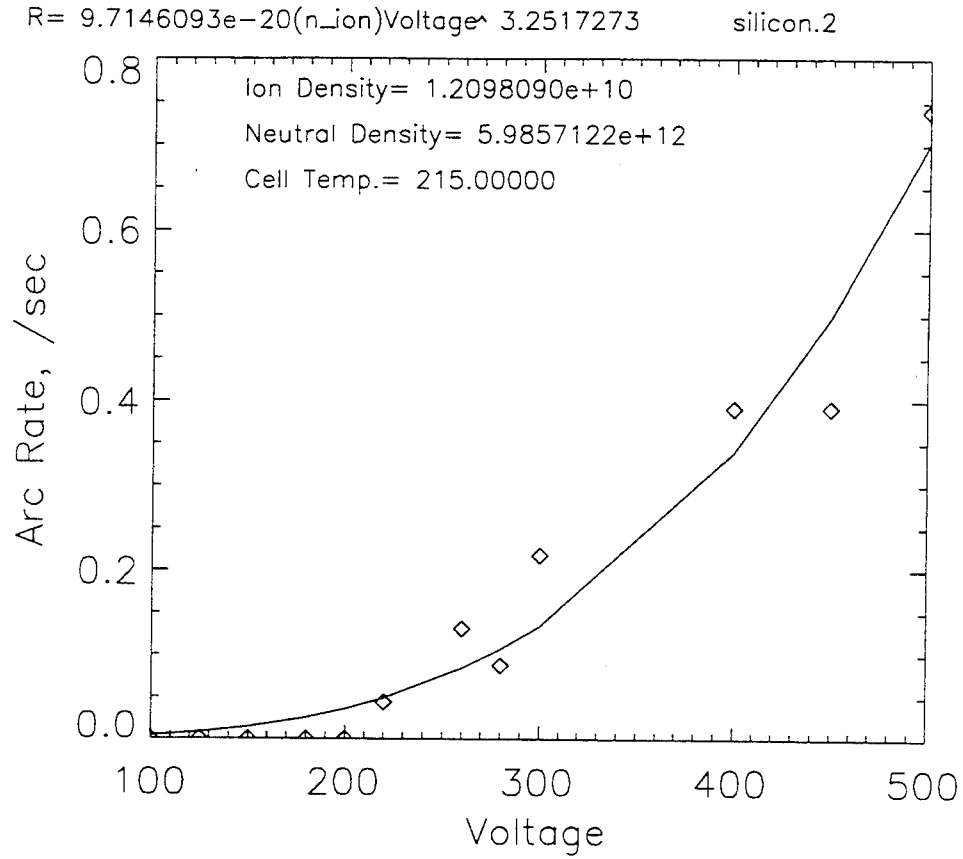


Figure 14: Voltage Power Law Fit to Array #2 Arc Rate

Ferguson for the PIX II data⁵, discussed in Chapter 1, was done, given by the equation

$$R = C_1 n_e (-V)^{C_2} \quad (41)$$

where n_e is the plasma density and C_1 and C_2 are coefficients found by the fit. An example of this is shown in Figure 14 for the silicon cells in array #2, which had approximately the same cell area as the PIX II cells. In the fits, the power of the voltage is on the order of 3, matching the results found by Ferguson. If this equation held, the coefficient C_1 would be independent of the plasma density. Preliminary studies, however, indicate that this may not be the case, implying that the arc rate is not linear with plasma density in the regime examined.

Another type of correlation between arc rate and voltage is motivated by the model used in the simulations. Because of the need to numerically calculate the charging times for the arcs, a closed form equation for the arc rate is not given by the model. However, by assuming a constant secondary electron yield, a form of the solution is implied by Eq. (28). It should be

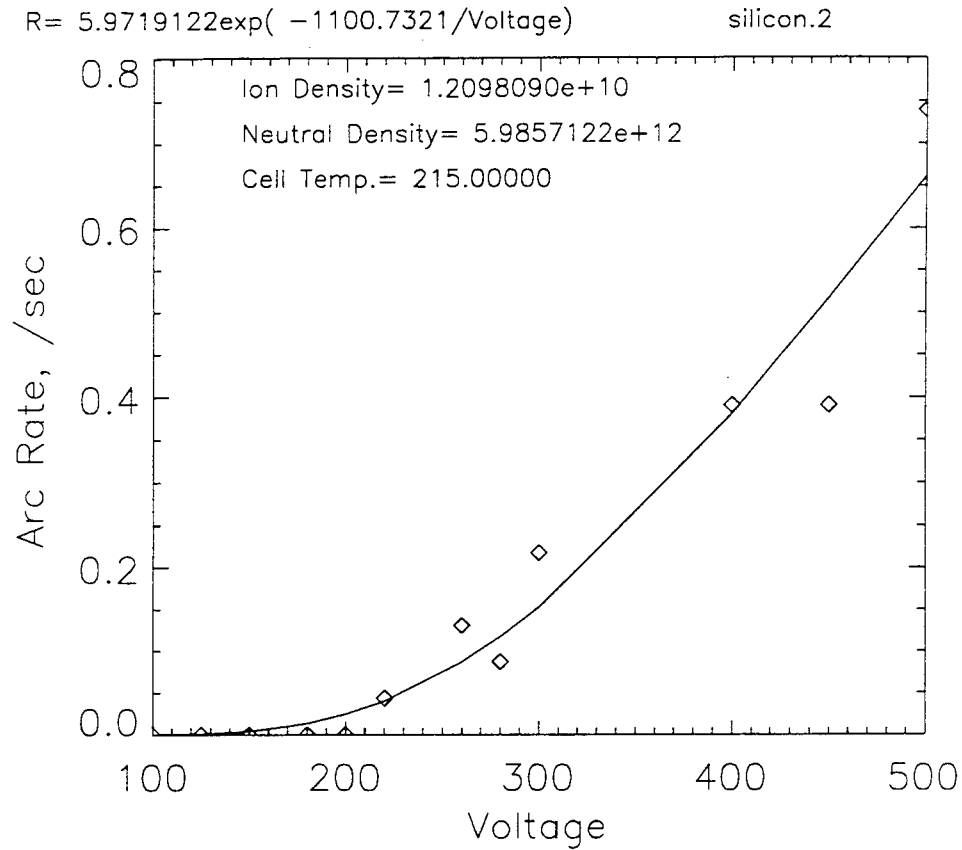


Figure 15: Voltage Exponential Fit to Array #2 Arc Rate

noted that this equation is combination of a linear function of V_e and an exponential function of V_e , where V_e is the voltage which the dielectric charges up to when EFEE charging is initiated, and not explicitly a function of the bias voltage. Neglecting this, and assuming that the exponential term of the equation was dominating, fits were made to the data with the form

$$R = C_1 \exp(C_2/V_{bias}) \quad (42)$$

where C_1 and C_2 are the coefficients found by the fit. Based on the typical values of the parameters in Eq. (28), C_1 is expected to be on the order of 10, while C_2 is expected to be on the order of -1000's. An example of this fit, using the same simulated data as for the fit above, is shown in Figure 15. The coefficients found in the fit match those expected from the model.

This data analysis software will be used to analyze the actual flight data to find the correlations between the arc rate and the various environmental and operational parameters

experienced by the arrays during the PASP Plus experiment.

Chapter 5

Conclusions

As space systems demand higher power levels, high voltage solar arrays will be used to meet these needs. This will result in more significant interactions taking place between the ambient space plasma environment and the arrays. Arcing has been observed to be one of these interactions for high negative voltage operation, simulated in experiments by biasing. Since this arcing can be detrimental to the operation of the spacecraft and can damage the arrays themselves, it is necessary to be able to understand the process leading to the arcing and be able to predict arcing on arrays operating in space.

The model used in this research to explain the arcing process is that developed by Cho and Hastings³. Previously, a semi-analytic model was created to predict the arcing rates on highly negative biased solar arrays, as discussed in Chapter 2. This model was then modified to be more physically accurate and to be able to predict the arcing on the conventional cells of the PASP Plus experiment.

In Chapter 3, the modifications made to the arc rate code were discussed. The first modification was to not use the assumption of a constant secondary electron yield. This resulted in a non-linear differential equation which had to be solved numerically to get the EFEE charging time, instead of the previous case where a closed form solution was found. While this is more computationally intensive, it is also more physically accurate and results in shorter electric field run-away times. Also included in the new code was the analysis of the desorbed neutral density criterion for breakdown. In previous work by Cho, the surface neutral density was assumed to be at the steady state value, while subsequent work by Mong²² neglected this criterion altogether and assumed that the neutral density was always sufficient for breakdown. The steady state assumption is only valid if the interval between arcs is sufficiently large that the surface has time to recharge the neutrals from the ambient, which may not be the case. By neglecting the criterion, Mong found the upper bound for the "big arcs", which are cases where breakdown occurs. In this work, the neutral density criterion is enforced, with the surface neutral density calculated time accurately.

The addition of "small arcs" was also made, which are cases where the field runs away but the desorbed neutral density is less than the critical density for breakdown. These small arcs would show up as detectable current pulses up to tens of milliamps, which are generally much smaller than those of big arcs. The code was also modified to allow the data describing the environment to be input at one second intervals, instead of assuming to be constant, to allow the simulation of the PASP Plus experiment throughout the orbit.

This code was then used to predict the arcing for the conventional cells aboard PASP Plus. The simulations showed that arc rates up approximately 4.3 arcs/second would be seen, with the thin cells showing more arcing activity than the thick cells. Expected arcing onset voltages were also found, ranging from -125 volts for the thin cells up to -180 and -200 volts for the thick silicon and GaAs/Ge cells, respectively. These predictions were then used to develop tools to look for correlations in the arc rate with the various environmental and operational parameters. Possible correlations examined for the arc rate with voltage include both a power law relation with voltage, as expressed by Ferguson for the PIX II flight data⁵, and an exponential relation as implied by the model by Cho and Hastings³. This software will be used to find the correlations for the arc rate from the actual flight data when it becomes available.

Bibliography

- [1] S. F. Adams, "Photovoltaic Array Space Power Plus Diagnostics Flight Experiment: Pre-Flight Description of Experimental Photovoltaic Modules", Technical Report WL-TR-92-2080, Wright Laboratory, 1992.
- [2] YA. L. Al'Pert. *The Near-Earth and Interplanetary Plasma*. Vol. 1, Cambridge University Press, 1983, pp. 22-24.
- [3] M. Cho, "Arcing on High Voltage Solar Arrays in Low Earth Orbit: Theory and Computer Particle Simulation," Ph.D. Thesis, M.I.T., 1992.
- [4] M. Cho and D. E. Hastings, "Dielectric Charging Processes and Arcing Rates of High Voltage Solar Arrays", *Journal of Spacecraft and Rockets*, Vol. 28, pp. 698-706, 1991.
- [5] Ferguson D. C., "The Voltage Threshold for Arcing for Solar Cells in LEO-Flight and Ground Test Results", NASA TM-87259, March 1986.
- [6] H. Fujii, Y. Shibuya, T. Abe, K. Ijichi, R. Kasai, and K. Kuriki, "Laboratory Simulation of Plasma Interaction with High Voltage Solar Arrays", *Proceedings of the 15th International Symposium on Space Technology Science*, Kanagawa, Japan, 1986.
- [7] N. T. Grier and N. John Stevens, "Plasma Interaction Experiment (PIX) Flight Results", *Spacecraft Charging Technology 1978*, NASA CP-2071, pp. 295-314.
- [8] N. T. Grier, "Plasma Interaction Experiment II: Laboratory and Flight Results", *Spacecraft Environment Interactions Technology Conference*, 1983, NASA CP-2359, pp. 333-348.
- [9] O. Hachenberg and W. Brauer, "Secondary Electron Emission from Solids", *Advancement in Electronics and Electron Physics*, Vol. 11, pp. 413-499, 1959.
- [10] D.E. Hastings and M. Cho, "Ion Drag for a Negatively Biased Solar Array in Low Earth Orbit", *Journal of Spacecraft and Rockets*, Vol. 27, pp. 279-284, 1990.

- [11] D. E. Hastings, M. Cho, and H. Kuninaka, "The Arcing Rate for a High Voltage Solar Array: Theory, Experiments and Predictions", *Journal of Spacecraft and Rockets*, Vol. 29, pp. 538-554, 1992.
- [12] D. E. Hastings, G. Weyl and D. Kaufman, "The Threshold Voltage for Arcing on Negatively Biased Solar Arrays", *Journal of Spacecraft and Rockets*, Vol. 27, pp. 539-544, 1990.
- [13] B. G. Herron, J. R. Bayless and J. D. Worden, "High Voltage Solar Array Technology", *Journal of Spacecraft and Rockets*, Vol. 10, pp. 457, 1973.
- [14] G. B. Hillard and D. C. Ferguson, "The Solar Array Module Plasma Interaction Experiment: Technical Requirements Document", NASA TM-105660, 1992.
- [15] G. B. Hillard and D. C. Ferguson, "The Solar Array Module Plasma Interactions Experiment (SAMPIE): Science and Technology Objectives", to be published in the *Journal of Spacecraft and Rockets*.
- [16] R. W. Hockney and J. W. Eastwood. *Computer Simulation Using Particles*. McGraw-Hill, USA, 1981.
- [17] G. T. Inouye and R. C. Chaky, "Enhanced Electron Emission from Positive Dielectric/Negative Metal Configurations on Spacecraft", *IEEE Trans. Nuc. Sci.*, Vol. NS-29, No. 6, December 1982, pp. 1589-1593.
- [18] G. A. Jongeward, I. Katz, M. J. Mandell and D. E. Parks, "The Role of Unneutralized Surface Ions in Negative Potential Arcing", presented at the 1985 IEEE 22nd Annual Conference, NSRE.
- [19] R. V. Latham, *High Voltage Vacuum Insulation: The Physical Basis*. Academic Press, London, England, 1981.
- [20] R. V. Latham, "Prebreakdown Electron Emission", *IEEE Transactions on Electrical Insulation*, Vol. EI-18, June 1983.
- [21] P. Leung, "Characterization of EMI Generated by the Discharge of a 'Volt' Solar Array", Technical Report CR-176537, NASA, November 1985.
- [22] R. L. Mong, "Arcing Mitigation and Predictions for High Voltage Solar Arrays", S.M. Thesis, M.I.T., 1993.
- [23] "PASP Plus Data Processing and Analysis Meeting", Phillips Laboratory, US Air Force, Jan 20, 1994.

- [24] "PASP Plus Experiment Specification," Phillips Laboratory, Jan 17, 1991.
- [25] D. E. Parks, G. Jongeward, I. Katz and V. A. Davis, "Threshold-Determining Mechanisms for Discharges in High-Voltage Solar Arrays", *Journal of Spacecraft and Rockets*, Vol. 24, pp. 367-371, 1987.
- [26] W. H. Press, B. P. Flannery, S. A. Teukolsky, and W. T. Vetterling, *Numerical Recipes The Art of Scientific Computing*. Cambridge University Press, Cambridge, Englasnd, 1986.
- [27] P. S. Severance and D. A. Guidice, "Investigation of Space Environmental Effects on Advanced Solar Arrays", Phillips Laboratory, presented at Phillips Laboratory *Second Annual Technical Interchange Symposium*, Albuquerque NM, 14 July 1993.
- [28] D. B. Snyder, "Discharges on a Negatively Biased Solar Cell Array in a Charged Particle Environment", *Spacecraft Environment Interactions Technology Conference*, 1983, NASA CP-2359, pp. 379-388.
- [29] D. B. Snyder and E. Tyree, "The Effect of Plasma on Solar Cell Array Arc Characteristics", Technical Report TM-86887, NASA, 1985.
- [30] N. J. Stevens, "Review of Interactions of Large Space Structures with the Environment, Space Systems and their Interactions with Earth's Space Environment", *Progress in Aeronautics and Astronautics*", Vol. 71, AIAA, Washington D. C., pp. 437-454, 1980.
- [31] H. Thiemann and K. Bogus, "Anomalous Current Collection and Arcing of Solar-Cell Modules in a Simulated High-Density Low-Earth-Orbit Plasma, *ESA Journal*, Vol. 10, pp. 43-57, 1986.
- [32] H. Thieman, R. W. Schunk and K. Bogus, "Where do negatively biased solar arrays arc?", *Journal of Spacecraft and Rockets*, Vol. 27, pp. 563-565, 1990.